Title	Planetary nebulae detected in the Spitzer Space Telescope GLIMPSE 3D Legacy Survey
Author(s)	Zhang, Y; Hsia, CH; Kwok, S
Citation	Astrophysical Journal, 2012, v. 745 n. 1, article no. 59
Issued Date	2012
URL	http://hdl.handle.net/10722/179719
Rights	Creative Commons: Attribution 3.0 Hong Kong License

Planetary Nebulae Detected in the *Spitzer Space Telescope* GLIMPSE 3D Legacy Survey

Yong Zhang, Chih-Hao Hsia, Sun Kwok

Department of Physics, The University of Hong Kong, Hong Kong

zhangy96@hku.hk,xiazh@hku.hk,sunkwok@hku.hk

ABSTRACT

We used the data from the *Spitzer* Legacy Infrared Mid-Plane Survey Extraordinaire (GLIMPSE) to investigate the mid-infrared (MIR) properties of planetary nebulae (PNs) and PN candidates. In previous studies of GLIMPSE I & II data, we have shown that these MIR data are very useful in distinguishing PNs from other emission-line objects. In the present paper, we focus on the PNs in the field of the GLIMPSE 3D survey, which has a more extensive latitude coverage. We found a total of 90 Macquarie-AAO-Strasbourg (MASH) and MASH II PNs and 101 known PNs to have visible MIR counterparts in the GLIMPSE 3D survey area. The images and photometry of these PNs are presented. Combining the derived IRAC photometry at 3.6, 4.5, 5.8, 8.0 μm with the existing photometric measurements from other infrared catalogs, we are able to construct spectral energy distributions (SEDs) of these PNs. Among the most notable objects in this survey is the PN M1-41, whose GLIMPSE 3D image reveals a large bipolar structure of more than 3 arcmin in extent.

Subject headings: infrared: ISM — planetary nebulae: general — stars: AGB and post-AGB

1. INTRODUCTION

Planetary nebulae (PNs) are important tools for the study of stellar nucleosynthesis and galactic chemical evolution. However, due to interstellar extinction, current optical census of Galactic PNs is highly incomplete, and some compact H II regions might have been mis-classified as PNs. The problem is particularly severe in the Galactic plane where the interstellar extinction is significant, and consequently the detections of PNs at optical bands are severely hampered. Unlike optical observations, infrared (IR) observations are

only marginally affected by interstellar extinction and observations of PNs in the IR is highly desirable.

PNs are bright in the IR due to their circumstellar dust component. The early prediction that the remnant of the circumstellar dust envelope from the asymptotic giant branch (AGB) progenitors should still be observable in the PN phase (Kwok 1982) has been confirmed by the *Infrared Astronomical Satellite* (*IRAS*) all-sky survey (Pottasch et al. 1984; Zhang & Kwok 1991). The peak of the infrared emission lies between 20-30 μm, corresponding to a color temperature of $\sim$100-150 K. Quite often a significant fraction of the energy output of PNs is emitted in the IR and mid-IR brightness has become a defining characteristics of PNs.

Although the structure of the ionized component of PNs is well determined by optical observations, early IR observations have too low spatial resolution to resolve the structures of the dust component of PNs. The recent *Spitzer Space Telescope* and the Galactic Legacy Infrared Mid-Plane Survey Extraordinaire (GLIMPSE; Benjamin et al. 2003, Churchwell et al. 2009) mapped the inner Galaxy at mid-infrared (MIR) 3.6 , 4.5, 5.8, and 8.0 μm using the Infrared Array Camera (IRAC; Fazio et al. 2004). With high resolution and sensitivity, the GLIMPSE data provide new insights into the nature of the nebular components contributing to the infrared emission of PNs. The GLIMPSE I & II images cover a total area of about 274 deg^2 of the Galactic plane and these data have been used for the studies of PNs (e.g. Cohen et al. 2007b, 2011; Phillips & Ramos-Larios 2008a,b, 2009; Ramos-Larios & Phillips 2008). Our research group has carried out systematic searches of PNs in the fields of GLIMPSE I & II (Kwok et al. 2008; Zhang & Kwok 2009). Our previous results show that the IR appearances of PNs might differ from their optical counterparts, and these IR images can help to distinguish between PNe and H II regions.

In the present work we present a study of PNs in the area of the GLIMPSE 3D survey. The GLIMPSE 3D program extends the GLIMPSE I & II coverage to higher latitude, where the IR background is not so bright as in the low-latitude regions. Although Quino-Mendoza et al. (2011) have investigated the IR properties of 24 PNs in the GLIMPSE 3D survey area, our sample is much larger (with a total of 191 PNs). This paper should be considered as a complement of our previous work (Kwok et al. 2008; Zhang & Kwok 2009).

2. OBSERVATIONS AND DATA REDUCTION

This study is primarily based on IRAC images, centered at approximately 3.6, 4.5, 5.8 and 8.0 μm, from the GLIMPSE 3D dataset (Meade et al. 2007). All the four bands were

simultaneously observed with a pixel resolution of $\sim 1.2''$. The GLIMPSE 3D survey extends the GLIMPSE I & II latitude coverage to $|b| < 3^\circ$ at nine selected strips above and below the Galactic plane (centered at $l = 10, 18.5, 25, 30, 330, 335, 341.5, 345$, and 350°), and to $|b| < 4.2^\circ$ in the center of the Galaxy ($|l| < 2^\circ$). The total area is about $120\,\mathrm{deg}^2$. Figure 1 shows the area coverage of the GLIMPSE 3D survey.

The GLIMPSE 3D data products are very similar to those of GLIMPSE I & II. The basic data calibration was performed by the Spitzer Science Center (SSC). The basic calibrated data were further processed using the GLIMPSE pipeline to correct for further instrumental artifacts, cross-identify and determine the flux densities and positions of point sources, and mosaic the images. Further details of the GLIMPSE archive and data processing can be found in Benjamin et al. (2003). The GLIMPSE 3D data products include a highly reliable Point Source Catalog (GLM3DC), a more complete Point Source Archive (GLM3DA), and mosaic images covering the survey areas.

The sample of PNs was taken in part from the MASH (Macquarie/AAO/Strasbourg Hα Planetary Galactic Catalogue) and MASH II catalogues (Parker et al. 2006; Miszalski et al. 2008), which contain over 1000 new faint PNs and PN candidates (hereafter, simply referred to as MASH PNs) discovered in the AAO/UKST Hα survey of the southern Galactic plane. The sample contains some of the most obscured PNs in the Galaxy. The survey area of GLIMPSE 3D survey is completely covered by the AAO/UKST Hα survey. Furthermore, we also searched for all the previously known PNs catalogued by Kohoutek (2001) within the GLIMPSE 3D survey area. These PNs are designated as "previously known PNs" in the following discussion.

We visually examined the IRAC images of all these PNs lying within the GLIMPSE 3D area. If a PN is visible in at least one of the bands, we measured its integrated fluxes using the same method as in our previous papers (Kwok et al. 2008; Zhang & Kwok 2009). Two apertures were employed to measure the on-source and background fluxes (F_{on} and F_{off}). In all the four IRAC bands, the apertures were put in the identical positions. We then obtained the sum of all the fluxes of sources in the point-source archive within each aperture ($F_{on,p}$ and $F_{off,p}$). Finally, the PN fluxes were determined from $(F_{on} - F_{on,p}) - (F_{off} - F_{off,p})$. For each PN, we measured the fluxes using several apertures with different sizes, and the adopted values are the average of all the measurements. From these repeated measurements, we estimate the typical error of the photometry to be 5%, and up to 30% for the sources with low surface brightness. Because the radii of these PNs are typically larger than $8''$, we made extended source aperture correction using the correction factors suggested by Jarrett[1].

[1]http://spider.ipac.caltech.edu/staff/jarrett/irac/calibration/ext_apercorr.html

We also used the 24 μm data taken by the Multiband Imaging Photometer for *Spitzer* (MIPS; Rieke et al. 2004). The data were retrieved from the *Spitzer* Legacy program MIPS Inner Galactic Plane Survey (MIPSGAL). The MIPSGAL survey only has a small overlap in Galactic coverage with the GLIMPSE 3D survey. We determined the 24 μm fluxes of PNs using the same method as described above. To better explore nebular IR emission, we also made use of data from other IR archives, including the Two Micron All Sky Survey (2MASS), Deep Near Infrared Survey of the Southern Sky (DENIS), *Midcourse Space Experiment (MSX)*, the *IRAS* Point Source Catalogue (PSC), and specially the recently released AKARI Point Source Catalogues. In the AKARI All-Sky Survey (Murakami et al. 2007), the mid- and far-infrared images were obtained using the Infrared Camera (IRC) and Far-Infrared Surveyor (FIS) with spatial resolutions from 4″–61″. This study is also complemented by the 1.4 GHz radio fluxes taken from the NRAO VLA Sky Survey (NVSS; Condon et al. 1998).

3. RESULTS

We find that there are 228 MASH PNs in the GLIMPSE 3D area, among which 90 have clearly visible IRAC counterparts. The IRAC color composite images of these 90 PNs are shown in Figure 2, where we can easily see that the colors of these PNs are redder than those of the field stars. The notes on individual MASH PNs are given in Appendix A. The majority of the GLIMPSE 3D PNs have a size of < 30 arcsec. An inspection of Figure 2 clearly shows that the surface brightness of PNs is lower for larger PNs. For the MASH PNs that are very extended in the visible, their IR counterparts are difficult to find as the IR surface brightness are likely to fall below the IRAC detection limit.

Figure 1 shows that the spatial density of GLIMPSE 3D PNs is larger near the Galactic center. The detection rate (R_{IR}; the number of PNs having visible IR counterparts over the total number) of the GLIMPSE 3D PNs is 42%, larger than that of GLIMPSE I PNs which are located in the inner Galactic plane (Kwok et al. 2008). There are two main factors affecting the detection rate. Because the spatial distribution of the galactic dust is more diffuse than the ionized gas (which is more concentrated around hot stars), the effect of background emission on the detection of PNs at IR wavelengths is larger than that at optical. As a result, the bright IR background emission in the inner Galactic plane tends to decrease the R_{IR} value for the PNs close to the Galactic plane. On the other hand, unlike the Hα emission, the IR emission of PNs are hardly obscured by the interstellar dust. This tends to increase the R_{IR} value for the PNs near the Galactic plane where the interstellar extinction is larger than the outer regions. Indeed, as shown in Figure 1, the R_{IR} value in the regions of $|b| > 3^{\circ}$ is obviously smaller than that in the inner regions.

Among 107 previously known PNs, 101 have obvious IRAC counterparts. The high detection rate of previously known PNs is because they are in general brighter than the MASH PNs. We have carefully examined the GLIMPSE images of these 101 PNs, some show similar appearances as the optical images, and some only reveal the brighter central regions of the objects. Since they are often bright, some are saturated at the 8.0 μm band. The IRAC color composite images of 80 previously known PNs are presented in Figure 3, where we have excluded the saturated sources and those with non-detection in some bands. Quino-Mendoza et al. (2011) and Phillips & Ramos-Larios (2008a) presented the IRAC images of several known PNs, which are also excluded from Figure 3. We have also attempted to search for fainter outer structures but this effort is often hindered by strong infrared background. A previously known PN (M 1-41) is discussed in detail in Section 3.3.

3.1. SPECTRAL ENERGY DISTRIBUTIONS

The Spitzer IR fluxes of the GLIMPSE 3D PNs (including MASH and previously known PNs) are given in Table 1. About 37% of the GLIMPSE 3D PNs lie within the MIPSGAL/24 μm survey area. We find that the PNs are generally bright in the 24 μm band. We also search for the counterparts of these PNs in the AKARI All-Sky Survey. Table 2 gives the IRC and FIS fluxes of the GLIMPSE 3D PNs. Table 3 tabulates the magnitudes and fluxes from the DENIS, 2MASS, MSX, IRAS, and NVSS point source catalogues. In far-IR wavelengths, the spatial resolutions are low ($> 30''$), and the field stars cannot be resolved from the PNs. However, these PNs are much brighter than the surrounding stars at longer wavelengths. We infer that the contamination from the field stars to the far-IR fluxes should be negligible.

The SEDs of the GLIMPSE 3D PNs are constructed using the IR data from various databases (Figure 4). Since the IR data cover a wide wavelength range, we are able to derive the color temperatures of the dust component (e.g. see the case for NGC 6302). For most of the PNs, there is a rise in flux toward short wavelengths. This is due to the contributions from the photospheric and nebular bound-free emission (see Zhang & Kwok 1991 for a detailed discussion of SEDs of PNs) and in some cases from a warm dust component. For a few previously known PNs, the ISO and Spitzer/IRS spectra are available and these are plotted in Figure 4. In general, the spectra are in good agreement with the IR photometry data. The SEDs at long wavelengths ($> 10\,\mu$m) can be reasonably approximated by blackbodies of temperatures ~ 100 K, although the fluxes are likely to be contaminated by the emission from aromatic infrared bands (AIB) and emission lines.

Some PNs (e.g. H 1-17, H 1-32, H 1-40, M 2-23, and M 3-8) display prominent emission

features from amorphous silicate grains at 10 and 18 μm. All of them are non-Type I PNs and show an O-rich or mixed chemistry. The shapes and relative strengths of the two silicate features reflect the properties of the grains (e.g. Simpson 1991; O'Donnell 1994). For our sample, we find the strength ratios of the 18 and 10 μm ($R_{18/10}$) lie within the range of 3–8. The variation of the $R_{18/10}$ value may be due to different volume fractions of graphite or porosity of the grains in different sources (Vaidya & Gupta 2011). The derived $R_{18/10}$ values are about one order of magnitude higher than those suggested by models of Vaidya & Gupta (2011). However, we should mention that the uncertainties of subtracting the continuum may introduce large errors in measuring the strengths of the broad 18 μm feature. In Figure 5, we compare the scaled emissivities, $\kappa_\lambda = F_\lambda / B_\lambda(T)$, where $B_\lambda(T)$ is the blackbody function with a temperature of T. Although we do not find obvious difference in the feature profiles between different sources, the peak position of the 10 μm feature shifts from source to source, probably indicating to the variety of chemical composition of the grains (e.g. Min et al. 2007). The peak wavelength of the 10 μm feature ranges from 9.5 to 10.3 μm, and is shortest in H 1-40. We also find that H 1-40 has a mixed chemical composition and display strongest AIBs among the five PNs, supporting the conclusion of Vaidya & Gupta (2011) that the 10 μm feature shifts shortwards with graphite inclusions.

It is clear from the SEDs that in many PNs there are more than one dust component. While the cool dust components (dominant at wavelengths >10 μm) are well defined, there are excesses between 5 and 10 μm which is most likely to be due to a warm dust component (see examples of H 1-16, H 1-18, H 1-19, H 1-34 in Fig. 4). High spatial resolution observations are needed to identify the origin of this warm dust component.

3.2. Infrared COLORS

In Figure 6, we compare the distributions of GLIMPSE PNs in the [3.6] − [4.5] versus [5.8] − [8.0] color-color diagram. We do not find obvious differences between the colors of GLIMPSE 3D and GLIMPSE I/II PNs. Since a variety of emission mechanisms contribute toward the fluxes of the IRAC bands, we do not expect the color distribution to obey the blackbody law. These contributing factors include the cool dust component (probably the most dominant), the warm dust component, nebular gas emission, AIB emissions, and even photospheric emissions. Generally speaking, the sample PNs have colors to the right and below the blackbody line. For objects with IRAC fluxes dominated by cool dust emission, this trend can be explained by emissivity dependence on wavelength, which makes the longer wavelength bands fainter. Based on a study of 24 PNs, Quino-Mendoza et al. (2011) found that the previously known PNs tend to have a larger [5.8] − [8.0] color, and suggested that

this is an evolutionary consequence. However, our large sample study does not suggest such a trend (see Figure 6). For the PNs both in the samples of Quino-Mendoza et al. (2011) and this paper, we derive an average [5.8] − [8.0] color of 1.95, in agreement with the value of GLIMPSE I PNs obtained by Cohen et al. (2011), but lower than that by Quino-Mendoza et al. (2011) ($\sim$ 2.38). This might be in part due to different aperture correction factors used for extended source calibration. On the other hand, for the sources with large sizes, we only measure the bright central regions, probably resulting in different colors with those derived by Quino-Mendoza et al. (2011).

In Figure 7, we plot the [3.6] − [8.0] versus [8.0] − [24] color-color diagram. The [3.6] − [8.0] colors of GLIMPSE 3D PNs seem to be systematically smaller than those of GLIMPSE II PNs. This trend can also be seen in Figure 8 which gives the [3.6] and [8.0] versus [3.6] − [8.0] color-magnitude diagrams. In Figure 8 we can also find that the IR emissions of GLIMPSE 3D PNs are generally fainter than those of GLIMPSE I/II PNs. This is an indication that in the GLIMPSE I and II survey areas the detection of the PNs with intrinsically fainter IR emission is severely hampered by the bright background emission in the inner galactic plane. Based on GLIMPSE I data, Cohen et al. (2011) found that the MASH II PNs have a smaller [4.5] − [5.8] color than the MASH I PNs, and suggested that the MASH II PNs are more compact and younger. According to our measurements of GLIMPSE 3D, the average [4.5] − [5.8] values are 0.44 and 0.42 for MASH I and II PNs, respectively. Our results suggest that in the higher-latitude regions where there dust exctinction is lower, the bias in the discovery of MASH I and II PNs is smaller than that in the inner galactic plane.

Cohen et al. (2011) found a trend that the [4.5] − [5.8] and [5.8] − [8.0] color indices of GLIMPSE I PNs increases and decreases with PN age (proportional to intrinsic sizes of PNs), respectively, suggesting that the relatively strengths of AIBs change as PN age. In the GLIMPSE 3D survey area, most of the MASH PNs are compact and it is hard to estimate their sizes. To examine the relation between infrared colors and PN age, we divide our sample into two groups: I) small sources with clear boundary; II) extended sources or those with diffuse structures. We suppose that Groups I and II roughly represents young and more evloved PNs, respectively. There are 62 Groups I PNs and 22 Group II PNs. We derive [5.8] − [8.0] = 1.52 ± 0.57 for Group I and 1.47 ± 0.33 for Group II, in reasonable agreement with the conclusions of Cohen et al. (2011). However, giving such a large standard deviation, it is not possible to gain any further meaningful conclusion.

3.3. M 1-41

M 1-41 is one of the most interesting PNs within the GLIMPSE 3D survey area. Its central star has a energy-balance temperature of 142 400 K (Preite-Martínez et al. 1991), and is at a distance of about 1 kpc (Zhang 1995). Based on the radio morphology and infrared color, Zijlstra et al. (1990) suggested that this source is a mis-classified PN and is likely to be a H II region. However, a different conclusion was drawn by Bohigas (2001), who detected extended shock excited H_2 emission, and suggested that M 1-41 is a type I PN.

Figure 9 gives the IRAC image of M 1-41, which clearly reveals that this source is composed of a relatively bright central region and a pair of very extended faint lobes, suggesting that it is likely a nearby PN. The waist of the lobes is bright and visible in all the four bands. It is oriented at PA= 122° and has a size of $\sim 0.5'$. The lobes are visible only at 8 μm. Note that the photometry data given in Table 1-3 are only based on the central part of this PN. The northern lobe is incomplete because of the contamination from bright infrared background emission. The southern lobe has an extension of about $3.7'$ from the center. The long axis of the lobes is oriented at PA= 9° and is not perpendicular to the waist. It is clear that if the instrumental sensitivity is not sufficient to detect the extended lobes, the irregular central nebulosity would appear to be a H II regions, not a PN. This is a good example showing that poor dynamic range imaging can lead to mis-classification of the morphology of PNs.

Figure 4 shows that M 1-41 has a typical SED of PNs. The excess in the near infrared suggests that there is a warm dust component in addition to the main cool dust component peaking at 30 μm.

The appearance of M 1-41 suggests that the mass of the central part is much larger than that of lobes. The bipolar lobes only manifest themselves through their thin walls, outlining very low density cavities. The walls of the lobes can be the result of sweeping up of previously-ejected circumstellar materials by a later developed, fast, collimated wind. An alternative interpretation is that the bipolar cavities are created by radiation pressure blown out of the polar regions of an optically thick equatorial torus. In this scenario, the bipolar structure is not caused by the dynamical ejection, but by illumination. A similar scenario has been suggested to explain the formation of multipolar lobes of PNs (Kwok 2010; García-Segura 2010).

Except for M 1-41, we do not find PNs that obviously exhibit extremely extended structures. Most of the PNs can be clearly distinguished from the large-scale backgound emission. An exception is the bright IRAS source, PN 1824−1410. This object was first identified as a PN by Van de Steene et al. (1996) based on optical observations. Figure 10 shows its IRAC

image. The central part is a red and compact nebula, which is partially obscured by a foreground bright star. Its color and morphology are typical of the GLIMPSE 3D sample PNs. The IRAC image also reveals a more extended irregular emission region surrounding this source (about 1 arcmin in radius), at the west of which some filaments can be seen and are aligned approximately north-south. These IR structures are much more obvious compared to those shown by the Hα image of Van de Steene et al. (1996). Further investigation is needed to determine whether the extended irregular nebulosity is associated with this PN.

4. DISCUSSION

In order to investigate the contributions of AIBs to the IRAC bands we examine the relation between the 5.8μm/4.5μm and 8.0μm/4.5μm flux ratios for the GLIMPSE 3D PNs (Figure 11). It is clear that a positive correlation exists, and the distribution of the objects does not follow the blackbody curve. The AIBs at 6.2 and 7.7 μm can contribute to the 5.8 and 8.0 μm bands, respectively. As the 4.5 μm band has no contribution from AIBs, the positive correlation might reflect the correlation between the 6.2 and 7.7 μm AIB strengths. Figure 11 also suggests that the contributions from AIB emission to the 8.0 μm band is stronger than that to the 5.8 μm band. Another factor that contributes to the observed deviation to the blackbody curve is the contamination from the emission of ionized gas and/or central star to the 4.5 μm band. This point can be verified in Figure 2 where we do find that the 4.5 μm images are generally more centrally enhanced than the 5.8 and 8.0 μm ones. The effect can cause the data to shift towards higher temperature regions in this plot, and is more pronounced for the blackbody temperatures estimated by the 5.8μm/4.5μm flux ratio.

In order to examine the reliability of our flux measurements and the flux calibration of extended sources, we compare the IRAC 8.0 μm vs. *MSX* 8.3 μm and the MIPS 24 μm vs. *MSX* 21 μm integrated fluxes of The GLIMPSE 3D PNs in Figure 12. For these compact extended sources, the IRAC 8.0 μm and MIPS 24 μm fluxes are in good agreement with those of *MSX* 8.3 μm and 21 μm, respectively. We obtain average IRAC8.0 μm/*MSX*8.3 μm and MIPS24 μm/*MSX*21 μm flux ratios of 0.74 ± 0.28 and 0.99 ± 0.24, respectively. This is consistent with our previous results based on the GLIMPSE II PNs (Zhang & Kwok 2009), and suggests that our flux measurements are reliable. The average IRAC8.0 μm/*MSX*8.3 μm ratio also agrees with that of PNs obtained by Cohen et al. (2007b), but lower than that of H II regions deduced by Cohen et al. (2007a) (1.55 ± 0.15), suggesting that lower aperture correction factor should be applied to obtain the IRAC fluxes of more extended source. Figure 12 also indicates that for faint PNs the *MSX* 8.3 μm and 21 μm fluxes tend to be

underestimated. This might be due to the lower instrumental sensitivity of *MSX*.

As PNs expand and disperse into the interstellar medium, both the radio and infrared fluxes are expected to decline with age. It is therefore useful to see if a correlation exists between these two fluxes. Cohen et al. (2007b) claimed that previously known PNs and more evolved MASH PNs have different IR/radio flux ratio. Their conclusion, however, is not supported by subsequent studies (Cohen et al. 2011; Phillips & Márquez-Lugo 2011). In Figure 13 we compare the IR fluxes at 8.0 μm and 24 μm and the radio flux at 1.4 GHz from NVSS (Condon et al. 1998). There is no systematically difference between the IR/radio fluxes of MASH PNs and those of previously known PNs although MASH PNs are generally fainter. Figure 13 exhibits a weak correlation between the IR and radio fluxes. The distribution of objects in the 8.0 μm vs. 1.4 GHz flux plot are more scattered than that in the 24 μm and vs. 1.4 GHz plot, which might be attributed to the contamination from AIBs to the 8.0 μm band.

Phillips & Ramos-Larios (2009) compared the IR colors of Galactic PNs and those of Large Magellanic Could (LMC) PNs and found that the LMC PNs have lower [5.8]-[8.0] color indices. However, based on a study of different sample Cohen et al. (2011) argued that there is no statistically meaningful difference between these IR colors. Comparing the color-color plot (Figure 6) with Figure 6 of Phillips & Ramos-Larios (2009), we find that the color indices of GLIMPSE 3D PNs are approximately located within the same range with those of LMC PNs. The average [5.8]-[8.0] color indices of GLIMPSE 3D PNs is 1.62 which is not much different from the average value of the LMC PNs. Our results, therefore, support the conclusion of Cohen et al. (2011).

5. CONCLUSIONS

From the GLIMPSE 3D survey data, we have identified the IR counterparts of 191 galactic PNs. The images of 90 MASH PNs and 80 previous known PNs are presented and the SEDs of 83 PNs are constructed. The SEDs show clearly the importance of the dust component in PNs, as in many objects most of the energy is emitted in the dust component. The set of PN SEDs presented in this paper has helped us define the observational properties of PNs, allowing us to distinguish PN from other emission line objects.

Very extended bipolar lobes are discovered in the PN M1-41, suggesting that IR imaging is useful in finding outer structures of PNs which may be missed in optical observations.

One of the conclusions we have from this study is that the infrared images of the PNs are somewhat different from those in the visible. The obvious explanation is that the dust is

distributed differently from the ionized gas region. For example, bipolar nebulae would be visibly bright in the lobes but infrared bright in the equatorial regions. Interstellar extinction may also have affected the optical appearance of the objects.

The GLIMPSE IR data are useful to search for new PNs. The IRAC observations have resulted in the discovery of a new extremely redden PN G313.3+00.3 which is optically invisible (Cohen et al. 2005). This suggests that there may be many PNs hidden in the Galactic plane and the current census of Galactic PNs is far from being complete. The number of detected Galactic PNs is about one order of magnitude lower than the theoretically predicted value. We are starting a project to search for new (optically invisible) PNs in the GLIMPSE field. Our results will be reported elsewhere. The IR colors and SEDs of PNs presented in this paper will provide a useful diagnostics for the identification of new PNs.

We are grateful to Ed Churchwell and the GLIMPSE team for assistance in the processing and analysis of GLIMPSE survey data. We also thank Nico Koning for helpful discussions. This work is based on observations made with the *Spitzer Space Telescope*, which is operated by the Jet Propulsion Laboratory, California Institute of Technology, under a contract with NASA. This research has also made use of the NASA/IPAC Infrared Science Archive, which is operated by the Jet Propulsion Laboratory, California Institute of Technology, under contract with the National Aeronautics and Space Administration. Support for this work was provided by the Research Grants Council of the Hong Kong under grants HKU7032/09P and the Seed Funding Programme for Basic Research in HKU (200909159007).

A. INDIVIDUAL MASH PNs

PNG 000.4 + 04.4 .— This object, previously known as PN K 5-1, is a compact and low-excitation PN. It was first assigned as a possible PN by Preite-Martínez (1988) from the IRAS point Source Catalogue. The IRAC image shows that its IR emission is more extended and diffuse than its Hα counterpart (note that the optical images hereafter are based on the MASH catalogue). This might suggest that there exists extended dust and the nebula is ionized bounded. The SED indicates a color temperature of $T < 100\,\mathrm{K}$.

PNG 001.0 + 02.2 .— Its PN assignation can be confirmed by the IRAC color. The IR appearance is clearly more extended than its optical counterpart. The SED indicates a color temperature of $T < 150\,\mathrm{K}$.

PNG 001.1 + 02.2 .— The IRAC image shows that it has a compact and bright core.

We cannot find any difference between its IR and optical appearances. Its SED seems trace a component with a color temperature of about 600 K.

PNG 001.2 + 02.8 .— The low IR fluxes and compact appearance suggest that it is distant.

PNG 001.5 + 03.1 .— The IRAC image shows that it is diffuse and has an oval shape. The SED suggests that it is surrounded by dust with a temperature of about 100 K.

PNG 001.5 − 02.8 .— The IRAC image clearly shows that it consists of a bright core and an oval nebula. The nebula has a well-defined boundary and seems to be fainter along its major axis direction.

PNG 001.7 + 03.6 .— The Hα image shows that it is bright and compact. However, its IR counterpart is almost overwhelmed by the bright background emission.

PNG 001.7 − 02.6 .— It has weak hydrogen emission lines. The Hα image shows that "it is a very small faint round PN with enhanced E-W limbs/condensations". The limbs/condensations are not clear in the IRAC image.

PNG 002.1 + 02.6 .— The IRAC image shows that it is faint and has an oval shape.

PNG 002.2 + 01.7 .— Both Hα and IRAC images reveal that it is extremely compact.

PNG 002.3 − 01.7 .— It is a compact object. Parker et al. (2006) suggests that it might be an emission line star. Its IR emission is strong. The SED shows that it has a dust component with a color temperature of $T < 100$ K and is very likely to be a PN.

PNG 002.3 + 01.7 .— It has an oval shape. The Hα image shows that it has E-W limbs, which however is not clear in the IRAC image.

PNG 002.5 + 02.0 .— The Hα and IRAC images show that it is a faint compact source. The SED indicate to a color temperature of $T < 150$ K.

PNG 002.7 + 01.7 .— The Hα and IRAC images reveal a round appearance.

PNG 002.9−02.7 .— This source is also known as K 6-39 (Kohoutek 2002). It is compact and has a high excitation spectrum. The SED indicates a strong nebular bound-free emission and a dust component with a temperature of about 300 K.

PNG 003.1−01.6 .— The Hα image shows that it is an oval PN with faint outer detached halo to north. The IRAC image reveals a bright core with faint extended nebulosity.

PNG 003.4 − 01.8 .— The Hα image shows that it is a compact bipolar nebula. The bipolar structure, however, is not clear in the IRAC image.

PNG 004.2 − 02.5 .— The Hα and IRAC images reveal an oval shape.

PNG 004.3 + 01.8*a*.— It has an oval shape. The IRAC image shows a diffuse structure.

PNG 005.2 − 01.6 .— Both Hα and IRAC images show a very compact structure.

PNG 005.8 + 02.2*a*.— Its Hα appearance looks like a fuzzy elliptical nebula. The IRAC image reveal a bright core and a possible bipolar structure elongated along the NW-SE direction. The SED indicates a color temperature of < 300 K.

PNG 006.0 + 01.2 .— The IRAC image reveals an fuzzy oval shape. However, its 24 μm emission is quite strong.

PNG 006.1 + 01.5 .— This source is also known as K 6-33 (Kohoutek 2002). Both Hα and IRAC images show an X-shaped structure, suggesting that it might be a bipolar PN. The SED indicates a color temperature of about 100 K

PNG 006.1 − 02.1 .— Both Hα and IRAC images reveal a ring morphology.

PNG 006.9 + 01.5 .— The IRAC image shows that it is an extremely compact nebula.

PNG 007.5 − 02.4 .— The Hα image reveals an approximately circular nebula. The IRAC image shows a compact oval shape. The SED suggests a cold dust component with $T < 100$ K.

PNG 007.8 + 01.2 .— It is faint in optical image, but clearly seen by IRAC. It has a compact round morphology.

PNG 009.4 − 01.2 .— It shows a slightly oval shape. The IRAC appearance is very diffuse, and almost overwhelmed by the background emission. The SED shows that it has strong far-IR emission.

PNG 009.7 − 01.1 .— The Hα image shows a faint oval shape. It can be more clearly viem in the IRAC image. The SED suggests that its IR emission is dominated by thermal emission from cold dust with a temperature of < 50 K. This object may suffer from heavy extinction.

PNG 009.8−01.1 .— Both Hα and IRAC images reveal a bipolar structure with a bright core. Its IRAC appearance looks more centrally enhanced, suggesting the presence of a dust torus.

PNG 010.0 − 01.5 .— The Hα and IRAC images reveal a compace oval structure. The SED suggests a color temperature of <300 K.

PNG 010.2 + 02.4 .— The IRAC image reveals a roughly oval shape with some irregular

filaments.

PNG 010.2 + 02.7 .— This source is also known as IRAS 17552-1841 (Kohoutek 2001). The Hα and IRAC images reveal a circular morphology. The SED suggests strong far-infrared emission, implying the presence of cold dust.

PNG 010.6 + 02.4 .— The Hα image shows a round shape. The IRAC image reveals a slightly oval structure.

PNG 010.7 − 02.3 .— The Hα and IRAC images reveal a vaguely oval structure with a tail located on its southwest side.

PNG 011.0 + 01.4 .— The IRAC image reveals an oval structure with diffuse end of the major axis. The Hα shows the background emission, which is brighter in the IRAC image.

PNG 011.0 − 02.9 .— It appears a round shape. Its PN status was further confirmed by Boumis et al. (2006). The SED indicates the presence of cold dust with $T < 100\,\mathrm{K}$.

PNG 017.6 + 02.6 .— Its Hα appearance is compact. The IRAC image shows an oval shape with well-defined boundary. The SED reveals strong IR emission with a color temperature of $< 100\,\mathrm{K}$.

PNG 019.2−01.6 .— The Hα and IRAC images show a round shape. The SED indicates a color temperature of $< 300\,\mathrm{K}$.

PNG 024.2 + 01.8 .— The Hα and IRAC images show a roughly round structure with diffuse boundary.

PNG 025.6+02.8 .— The IRAC image reveal a bright compact core. The SED indicates a color temperature of about 150 K.

PNG 029.0 + 02.2 .— It is unresolved in the IRAC image. The SED indicates a color temperature of $< 100\,\mathrm{K}$.

PNG 029.2 − 01.8 .— The Hα image reveals a circular shape. In the IRAC image, it is heavily obscured by the bright background emission.

PNG 029.4 − 02.3 .— The IRAC image reveals a slightly oval shape although its Hα image appears to be round.

PNG 030.2 + 01.5 .— It is a compact object.

PNG 031.0 − 02.1 .— Both Hα and IRAC images reveal an elliptical shape.

PNG 329.8 − 03.0 .— The Hα image shows that it is a compact, bright oval nebula. The IRAC image reveal a faint ring with some irregular structures in the boundary. The

SED suggests strong far-IR emission from cold dust.

PNG 330.1 + 02.6 .— It is a compact source. The IRAC image reveals a bright core with a faint halo. The SED suggests a color temperature of about 150 K.

PNG 330.7 + 02.7 .— Its Hα emission is very faint. The IRAC image reveals a bright compact source.

PNG 334.0 + 02.4 .— The Hα and IRAC images exhibit an elliptical shape. The SED indicates the presence of cold dust with a color temperature of 60–150 K.

PNG 334.4 + 02.3 .— The Hα and IRAC images show an elliptical shape. The SED suggests a color temperature of about 150 K.

PNG 335.4 − 01.9 .— The Hα and IRAC images show an extended elliptical shape. The SED indicates the presence of cold dust with a color temperature of 60–150 K.

PNG 335.8 − 01.6 .— The IRAC image exhibits a bright compact source. Its SED is similar to those of other PNs, and suggests the presence of cold dust with a temperature of < 150 K.

PNG 335.9 − 01.3 .— The IRAC image reveal a bright compact source. Its SED clearly shows the nebular bound-free emssion, and dust emission with a color temperature of about 150 K.

PNG 341.7 + 02.6 .— It has an annular shape. The IRAC image shows that it is located inside a large cloud. The SED suggests a color temperature of < 300 K.

PNG 341.9 − 02.8 .— The IRAC image shows a compact source. The SED reveals a sharp increase in the wavelength of about 10 μm.

PNG 342.1 − 02.0 .— It is a very compact object.

PNG 344.0 + 02.5 .— The Hα and IRAC image reveal a compact structure. The SED suggests a color temperature of < 150 K.

PNG 344.4 + 01.8 .— The Hα image shows an elliptical morphology. The IRAC image reveals some filaments around the elliptical structure. The SED suggests a color temperature of < 300 K.

PNG 344.8 − 02.6 .— The Hα and IRAC image reveal a compact appearance.

PNG 345.8 + 02.4 .— The Hα and IRAC image reveal a compact structure. The SED suggests a color temperature of < 300 K.

PNG 345.8 + 02.7 .— Both Hα and IRAC images exhibit a oval ring with outer exten-

sions. The central star as revealed in the Hα image is invisible in the IRAC image. The SED suggests a color temperature of < 300 K.

PNG 349.6 − 02.1 .— The IRAC image shows a fuzzy structure with bright background emission.

PNG 350.4 + 02.0 .— This source is also known as IRAS 17092-3539 (Kohoutek 2001). The Hα and IRAC image reveal a faint elongated shape. The SED suggests a color temperature of ~ 100 K.

PNG 350.8 + 01.7 .— This source is also known as IRAS 17114-3532 (Kohoutek 2001). The Hα and IRAC image reveal a round appearance. The SED suggests the presence of cold dust with a temperature of ~ 100 K.

PNG 350.8 − 03.0 .— The IRAC image shows an extremely compact structure.

PNG 355.0 + 02.6 .— This source is also known as IRAS 17194-3137 (Kohoutek 2001). The IRAC image reveals a round appearance. The SED suggests a color temperature of ~ 100 K.

PNG 355.2 − 02.0 .— The Hα and IRAC image reveal a round appearance.

PNG 355.8 + 01.7 .— It is a very compact object.

PNG 356.0 − 01.8 .— The Hα and IRAC image reveal a compact and round appearance.

PNG 356.0 + 02.8 .— This source is also known as IRAS 17217-3040 (Kohoutek 2001). The Hα and IRAC image reveal a compact structure. The SED suggests a color temperature of < 150 K.

PNG 356.1 − 02.7 .— It is a compact object. The IRAC appearance looks more extended than the optical one.

PNG 356.2 + 02.5 .— The Hα and IRAC image reveal a compact structure. The SED suggests that its far-IR emission is quite strong.

PNG 356.2 + 02.7 .— The Hα and IRAC image reveal a compact structure.

PNG 356.3 − 02.6 .— It is a compact nebulosity behind a field star.

PNG 356.5 − 01.8 .— It is compact object. The SED may indicate the presence of a warm component, and thus it might be symbiotic star, as suggested by Parker et al. (2006).

PNG 356.6 + 02.3 .— The optical and IRAC images reveal a ring structure. Faint extentions are also displayed by the IRAC image.

PNG 357.3 − 02.0 .— The Hα image shows that it is a faint PN in obscured region. It appears as a bright round nebulosity in the IRAC image. The SED indicates a color temperature of ~ 100 K.

PNG 357.5 − 02.4 .— The Hα and IRAC images reveal a faint oval structure. The SED indicates a color temperature of < 100 K.

PNG 357.8 + 01.6 .— The Hα and IRAC images reveal a slightly extended structure. The Hα image also displays an outer arm, which however is not clear in the IRAC image.

PNG 357.9 + 01.7 .— It is a compact object.

PNG 358.0 − 02.4 .— The Hα and IRAC images show a faint compact structure.

PNG 358.1 + 02.3 .— The IRAC image reveals a bright core with slightly extended structure. Its SED differs from those of other PNs and suggests a color temperature of ~ 600 K. Thus it is unlikely to be a PN.

PNG 358.4 + 02.1 .— Its IR appearance is very fuzzy and almost overwhelmed by the background emission.

PNG 358.7 − 02.5 .— This source is also known as K 6-31 (Kohoutek 2002). The IRAC image shows a faint compact nebulosity.

PNG 359.2 − 02.4 .— The IRAC image shows a bright core with oval extentents.

PNG 359.4 + 02.3a.— The Hα and IRAC images show a compact structure.

PNG 359.6 + 04.3 .— The IRAC image exhibits a faint small nebulosity.

PNG 359.7 + 02.0 .— It is a compact object. The SED suggests a color temperature of < 150 K.

PNG 359.8 + 03.5 .— The Hα and IRAC images reveal an oval nebulosity.

REFERENCES

Bohigas, J. 2001, RevMexAA, 37, 237

Benjamin, R. A., et al. 2003, PASP, 115, 953

Boumis, P. et al. 2006, MNRAS, 367, 1551

Cohen, M. et al. 2005, ApJ, 627, 446

Cohen, M. et al. 2007a, MNRAS, 374, 979

Cohen, M. et al. 2007b, ApJ, 669, 343

Cohen, M., Parker, Q. A., Green, A., J., Miszalski, B., Frew, D., Murphy, T. 2011, MNRAS, 413, 514

Condon, J. J., & Kaplan, D. L. 1998, ApJS, 117, 361

Churchwell, E. et al. 2009, PASP, 121, 213

Fazio et al. 2004, ApJS, 154, 10

García-Segura, G. 2010, A&A, 520, L5

Kohoutek, L. 2001, A&A, 378, 843

Kohoutek, L. 2002, AN, 323, 57

Kwok, S. 1982, ApJ, 258, 280

Kwok, S, 2010, PASA, 27, 174

Kwok, S., Zhang, Y., Koning, N., Huang, H.-H., & Churchwell, E. 2008, ApJS, 174, 426

Meade, M. R. et al. 2007, GLIMPSE3D v1.0 Data Release (23 August, 2007)

Min, M., Waters, L. B. F. M., de Koter, A., Hovenier, J. W., Keller, L. P., & Markwick-Kemper, F. 2007, A&A, 462, 667

Miszalski, B., Parker, Q. A., Acker, A., Birkby, J. L., Frew, D. J., & Kovacevic, A. 2008, MNRAS, 384, 525

Murakami, H. et al. 2007, PASJ, 59, 369

O'Donnell, J. 1994, ApJ, 437, 262

Parker, Q. A. et al. 2006, MNRAS, 373, 79

Phillips, J. P., & Márquez-Lugo, R. A. 2011, RMxAA, 47, 83

Phillips, J. P. & Ramos-Larios, G. 2008a, MNRAS, 383, 1029

Phillips, J. P. & Ramos-Larios, G. 2008b, MNRAS, 386, 995

Phillips, J. P., & Ramos-Larios, G. 2009, MNRAS, 396, 1915

Pottasch, S.R., et al. 1984, A&A, 138, 10

Preite-Martínez, A. 1988, A&AS, 76, 317

Preite-Martínez, A., Acker, A., Koeppen, J. & Stenholm, B. 1991 A&AS, 88, 121,

Quino-Mendoza, J. A., Phillips, J. P., & Ramos-Larios, G. 2011, RMxAA, 47, 31

Ramos-Larios, G. & Phillips, J. P. 2008, MNRAS, 390, 1014

Rieke, G. H. et al. 2004, ApJS, 154, 25

Simpson, J. 1991, ApJ, 368, 570

Vaidya, D. B., & Gupta, R. 2011, A&A, 528, 57

Van de Steene, G. C., Jacoby, G. H., & Pottasch, S. R. 1996, A&AS, 118, 243

Zhang, C. Y. 1995, ApJS, 98, 659

Zhang, C. Y., & Kwok, S. 1991, A&A, 250, 179

Zhang, Y., & Kwok, S. 2009, ApJ, 706, 252

Zijlstra, A., Pottasch, S., & Bignell, C. 1990, A&AS, 82, 273

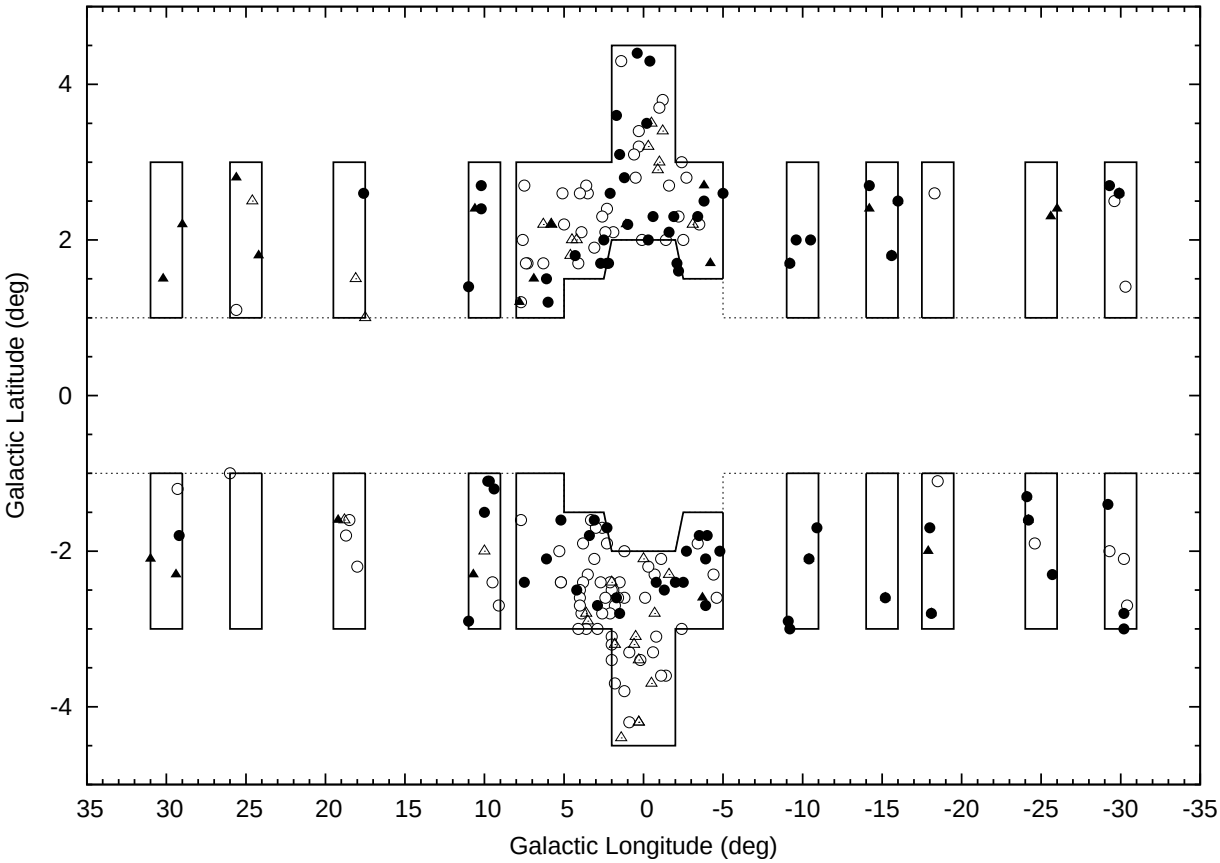

Fig. 1.— The sky coverage of GLIMPSE 3D survey (zones enclosed by solid lines). The dotted lines delineate the survey areas of GLIMPSE I & II. The locations of MASH and MASH II PNs lying within the GLIMPSE 3D survey area are shown by circles and triangles, respectively. The filled and open symbols respectively represent the PNs with and without IRAC counterparts.

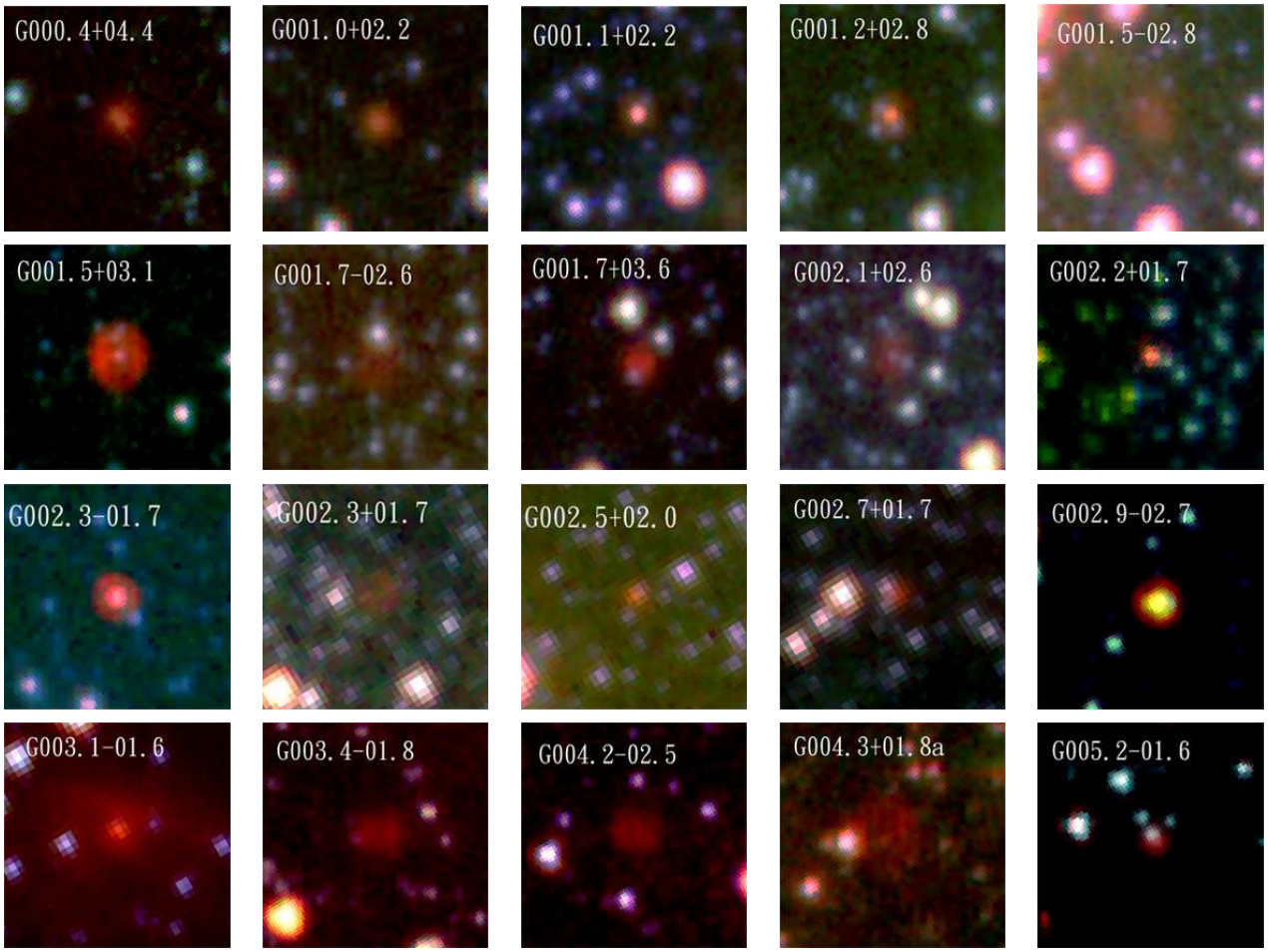

Fig. 2.— Composite-color images of 90 MASH PNs detected in the GLIMPSE 3D survey (abridged version). The images were made from the three IRAC bands: 3.6 μm (shown as blue), 5.8 μm (green), and 8.0 μm (red). Each panel covers an area of $40'' \times 40''$. North is up, and east is to the left.

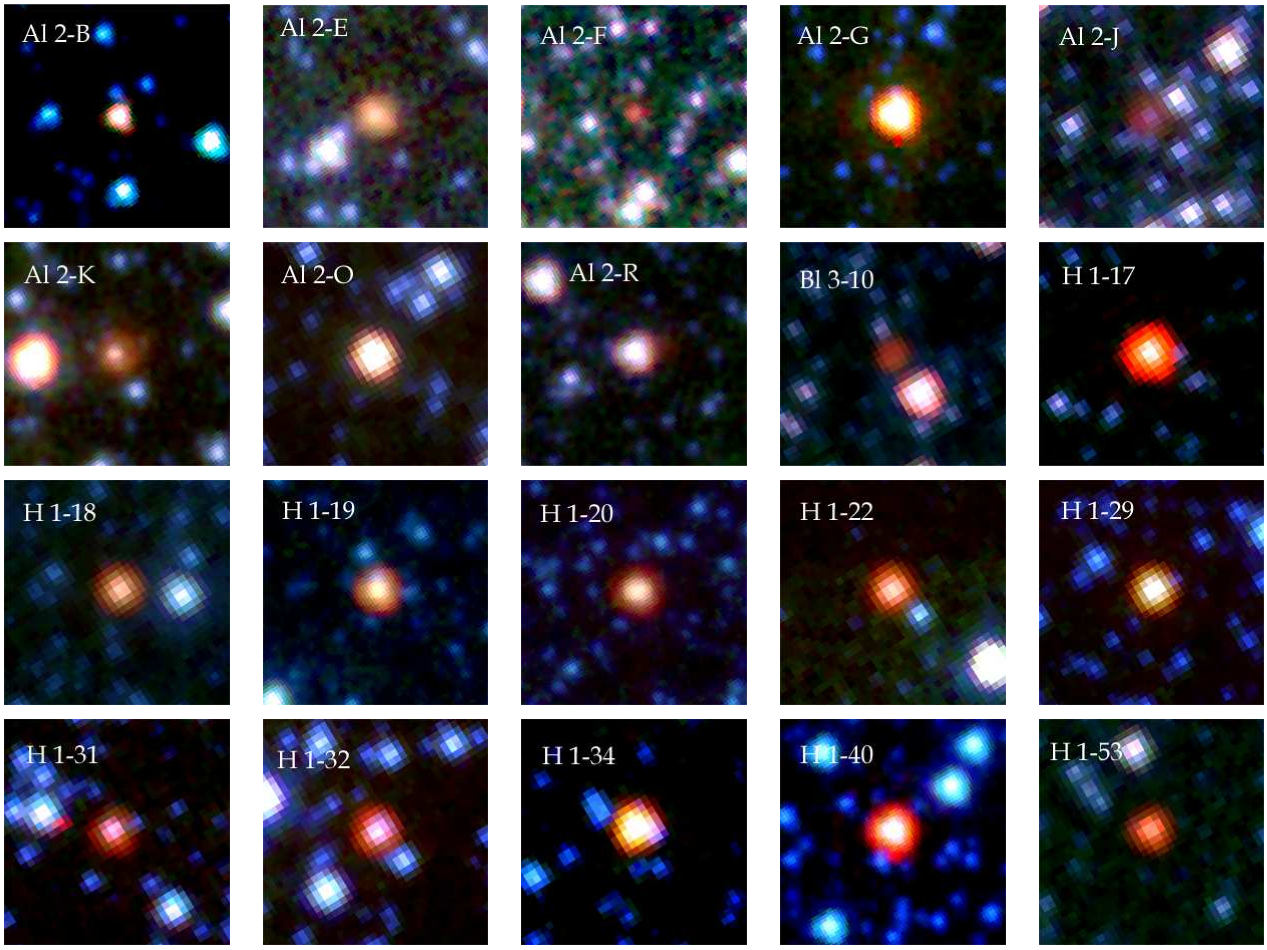

Fig. 3.— Composite-color images of 80 previously known PNs detected in the GLIMPSE 3D survey (abridged version). The images were made from the three IRAC bands: 3.6 μm (shown as blue) , 5.8 μm (green), and 8.0 μm (red). Except those marked, each panel covers an area of $40'' \times 40''$. North is up, and east is to the left.

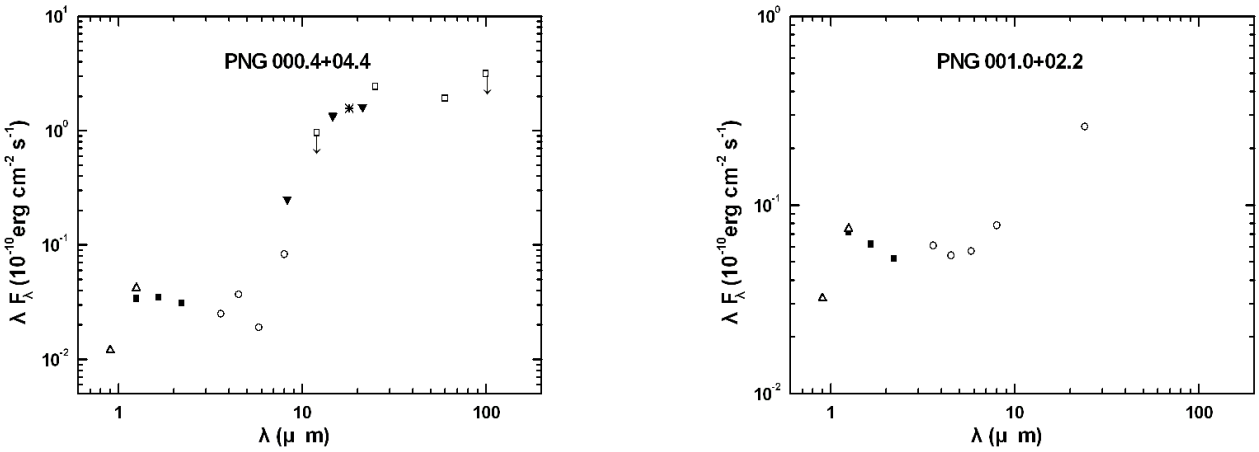

Fig. 4.— The SEDs of 83 PNs in the GLIMPSE 3D sample (abridged version). The open triangles, filled squares, open circles, open squares, filled triangles, and asterisks are from the DENIS, 2MASS, GLIMPSE/MIPSGAL, *IRAS*, *MSX*, and AKARI survey, respectively. The light asterisks represent the uncertain AKARI detections. The ISO and Spitzer spectra of some PNs are also overlaid. The dotted lines represent the blackbody curve with temperatures indicated.

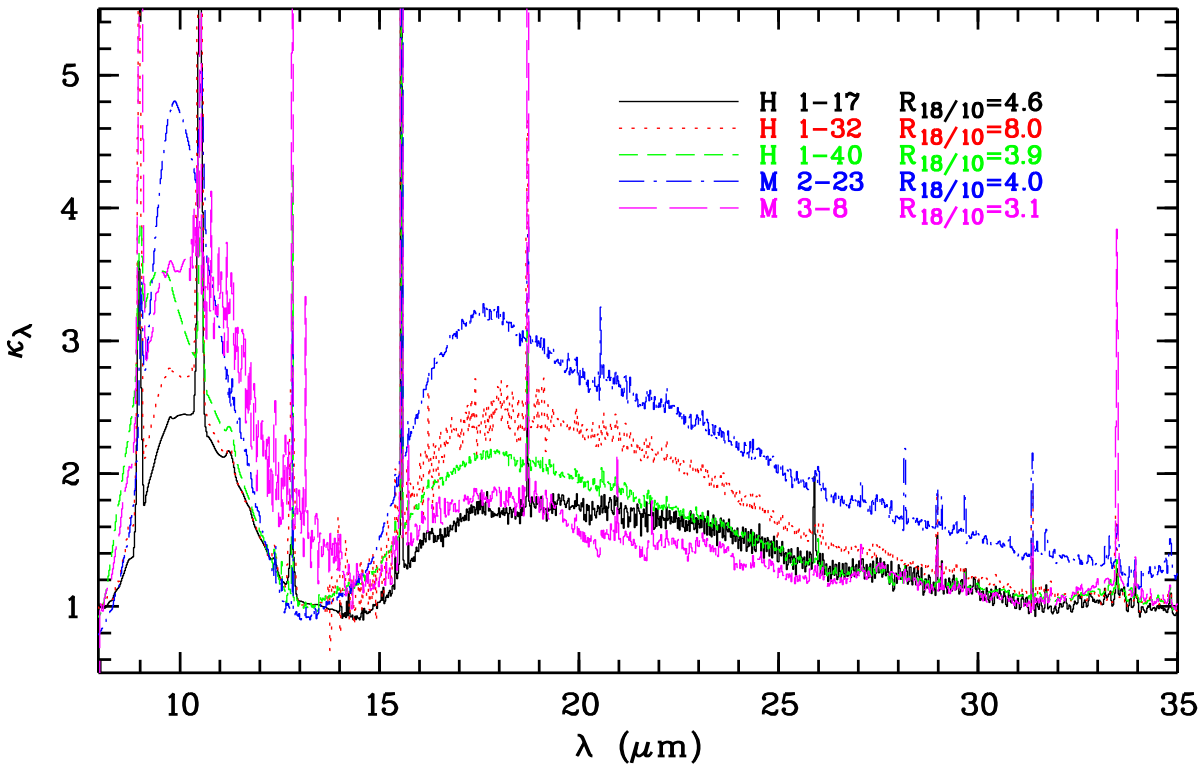

Fig. 5.— Emissivities of the PNs exhibiting strong 10 and 18 μm features.

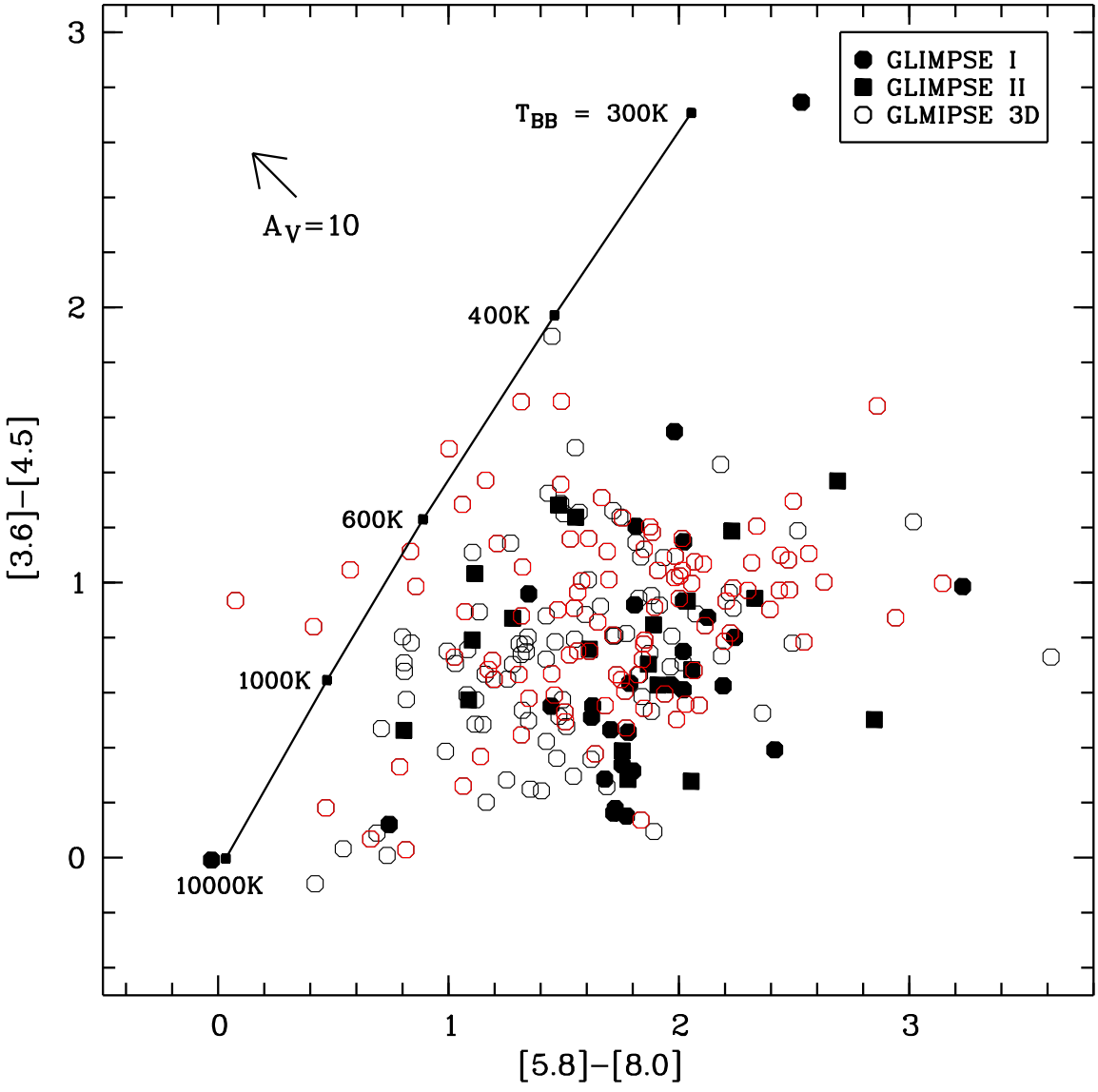

Fig. 6.— IRAC color-color plot ([3.6] − [4.5] vs. [5.8] − [8.0]) for 231 GLIMPSE PNs with good fluxes at all 4 IRAC bands. The red and black symbols denote the previously known and MASH PNs, respectively. The solid line is a track of blackbodies at temperatures $T_{\rm BB}$. The arrow in the upper left corner denotes a reddening vector of $A_v = 10$.

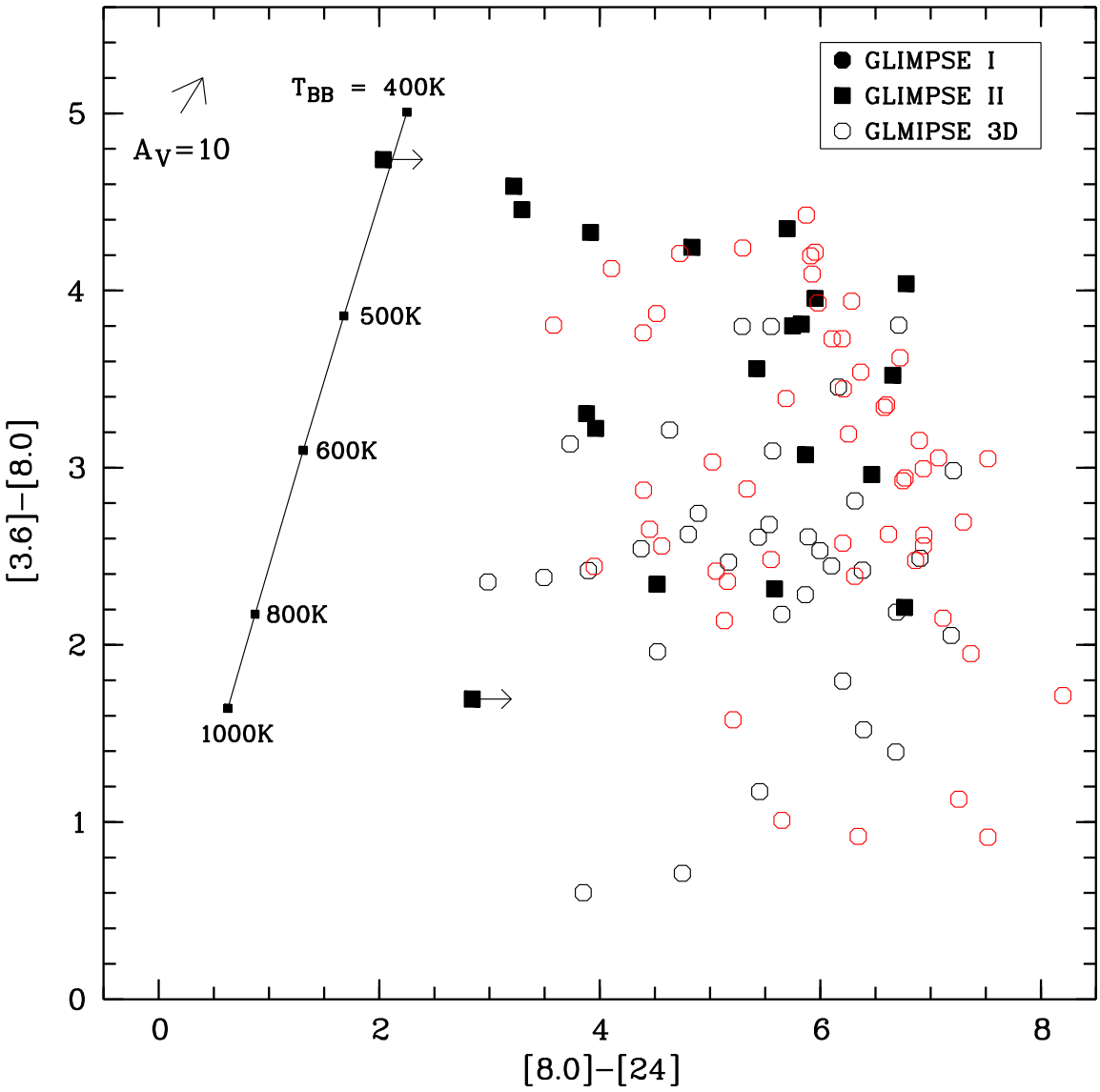

Fig. 7.— The $[3.6]-[8.0]$ versus $[8.0]-[24]$ color-color diagram for 106 GLIMPSE PNs with good fluxes at 3.6, 8.0, and 24 μm. Symbols are otherwise same as in Figure 6.

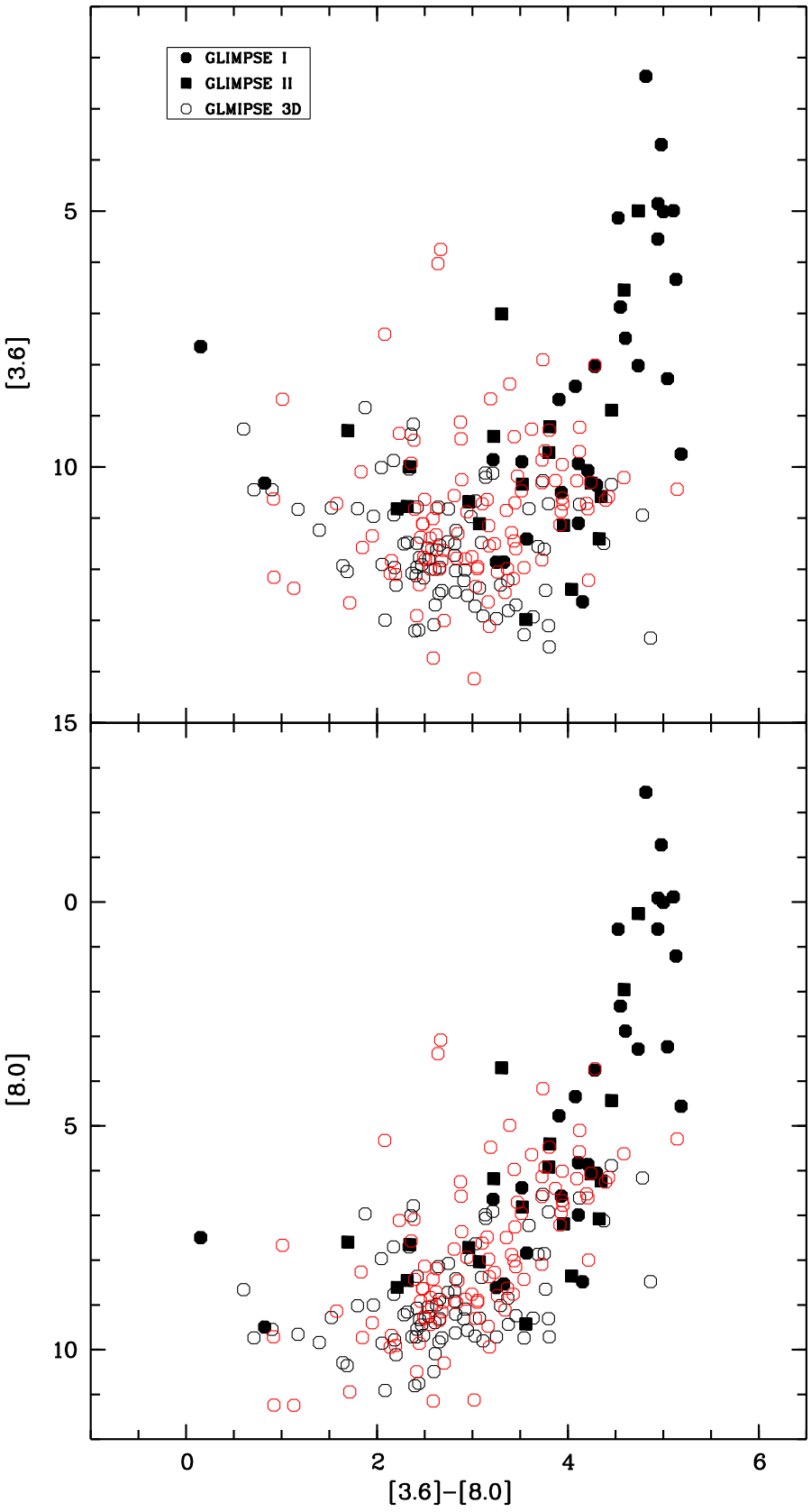

Fig. 8.— The [3.6] versus [3.6] − [8.0] (upper panel) and [8.0] versus [3.6] − [8.0] (lower panel) color-magnitude diagrams for 231 GLIMPSE PNs. Symbols are otherwise same as in Figure 6.

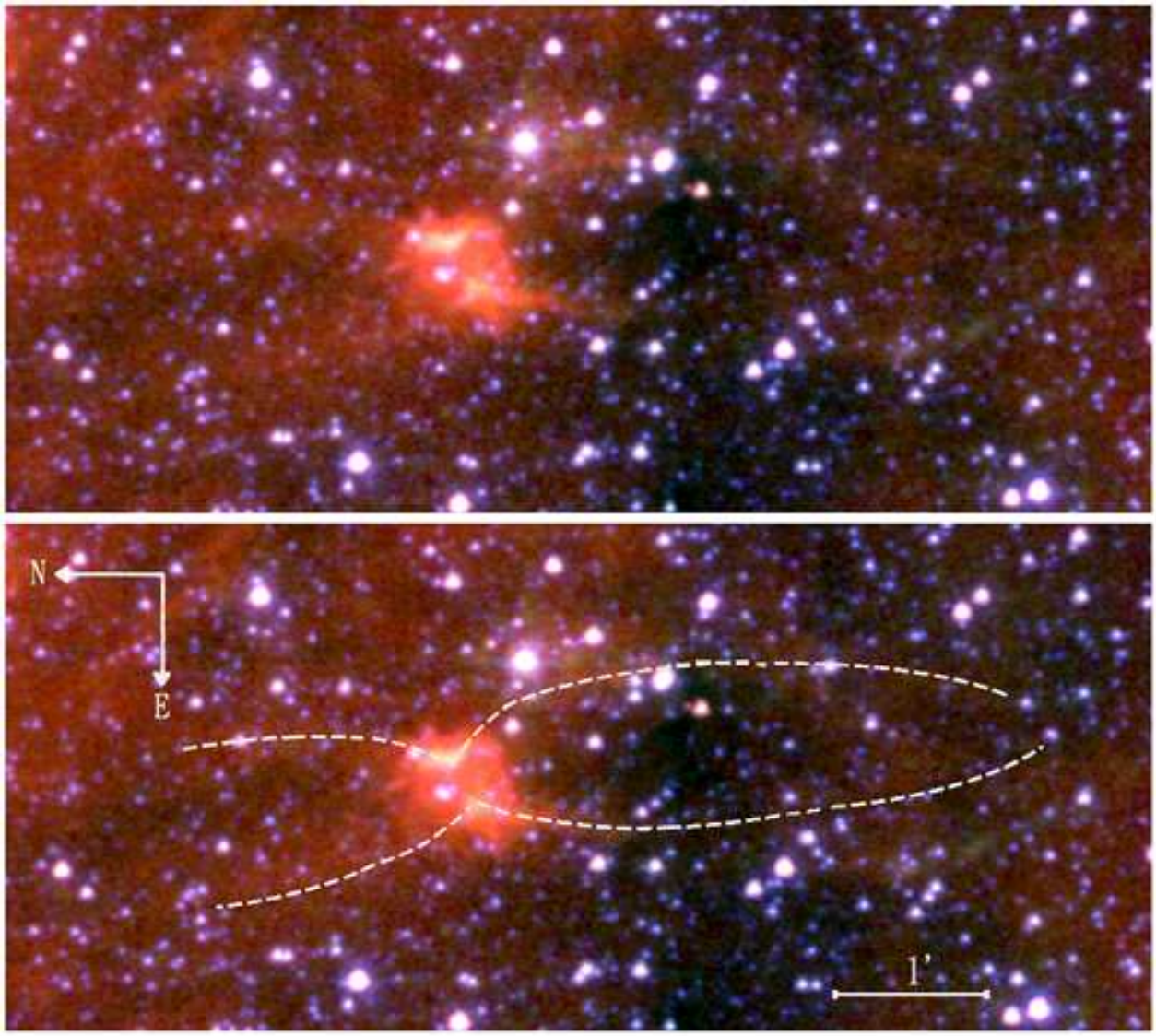

Fig. 9.— The IRAC image of M 1-41. The 3.6 μm is shown as blue, the 5.8 μm is shown as green, and the 8.0 μm is shown as red. The superimposed dashed lines are a sketch of the extended bipolar structures.

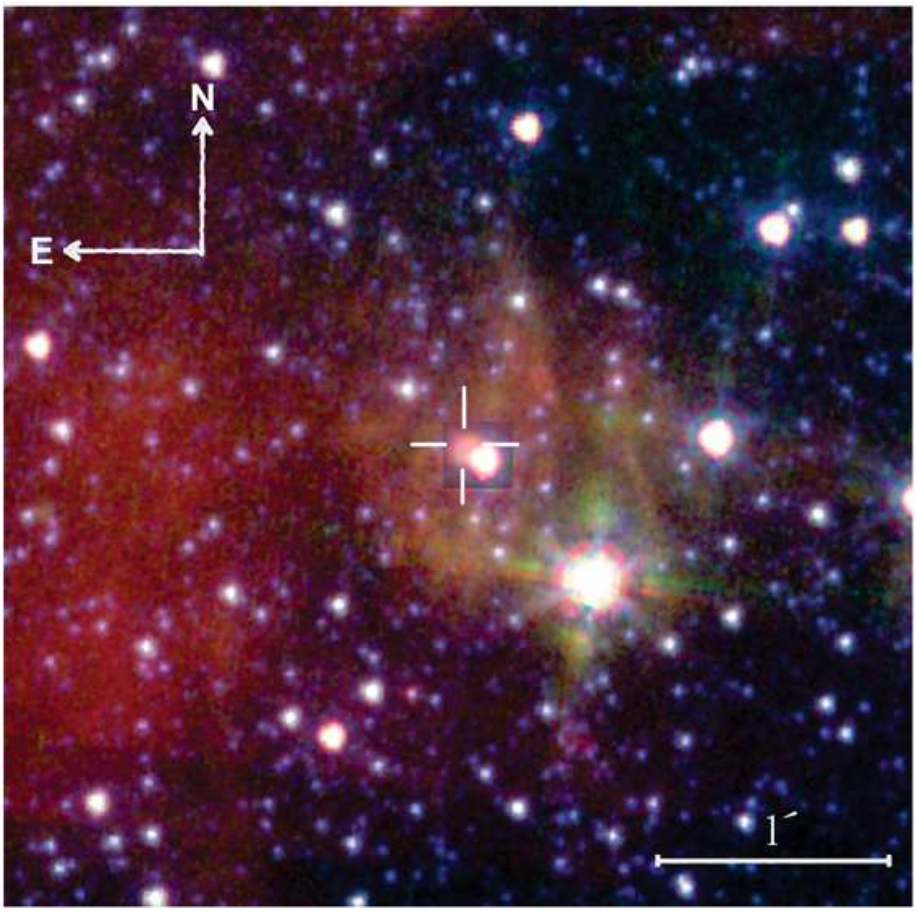

Fig. 10.— The IRAC image of PN 1824−1410. The 3.6 μm is shown as blue, the 5.8 μm is shown as green, and the 8.0 μm is shown as red. The position of the central part is marked.

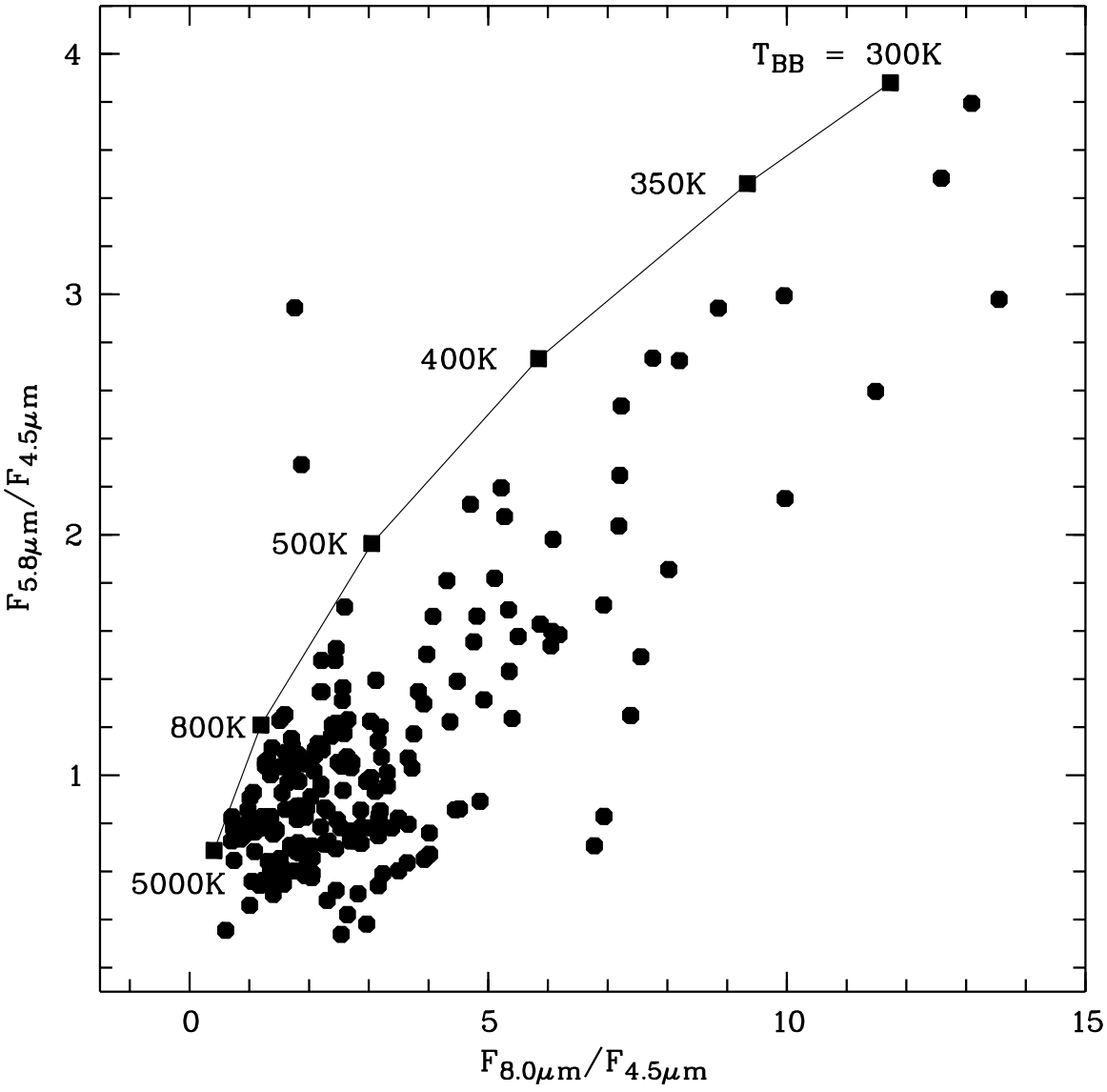

Fig. 11.— The 5.8 μm/4.5 μm flux ratios vs the 8.0 μm/4.5 μm flux ratios of 182 PNs in our sample. Nine objects are not plotted due to non-detection or saturated fluxes in one or more of the bands. The solid line is a track of blackbodies. Some blackbody temperatures are marked on the curve.

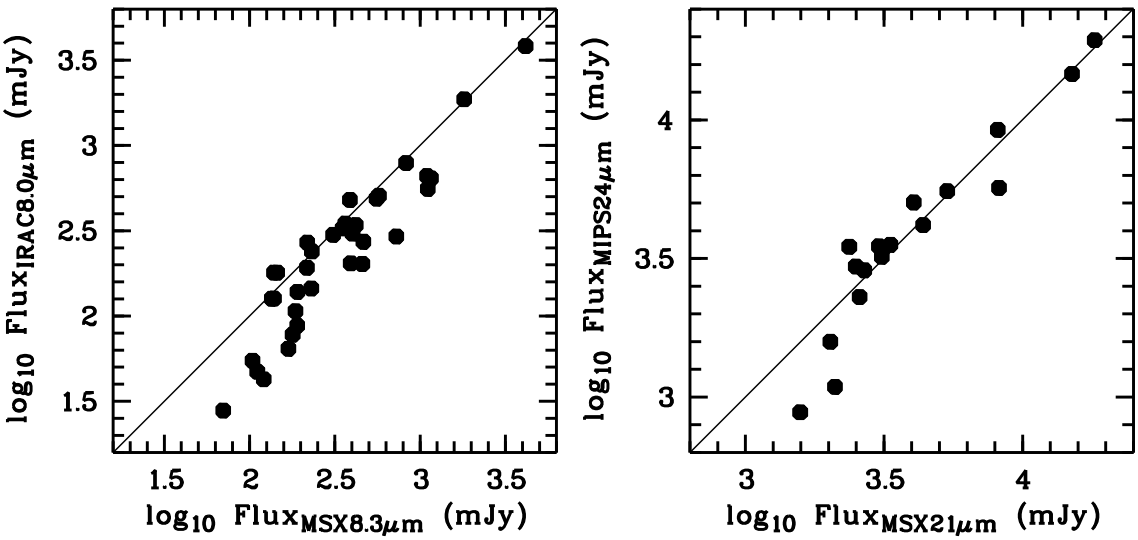

Fig. 12.— Left panel: IRAC 8.0 μm vs. *MSX* 8.3 μm integrated fluxes for 35 PNs. Right panel: MIPS 24 μm vs. *MSX* 21 μm integrated fluxes for 17 PNs. The solid line is a $y = x$ plot.

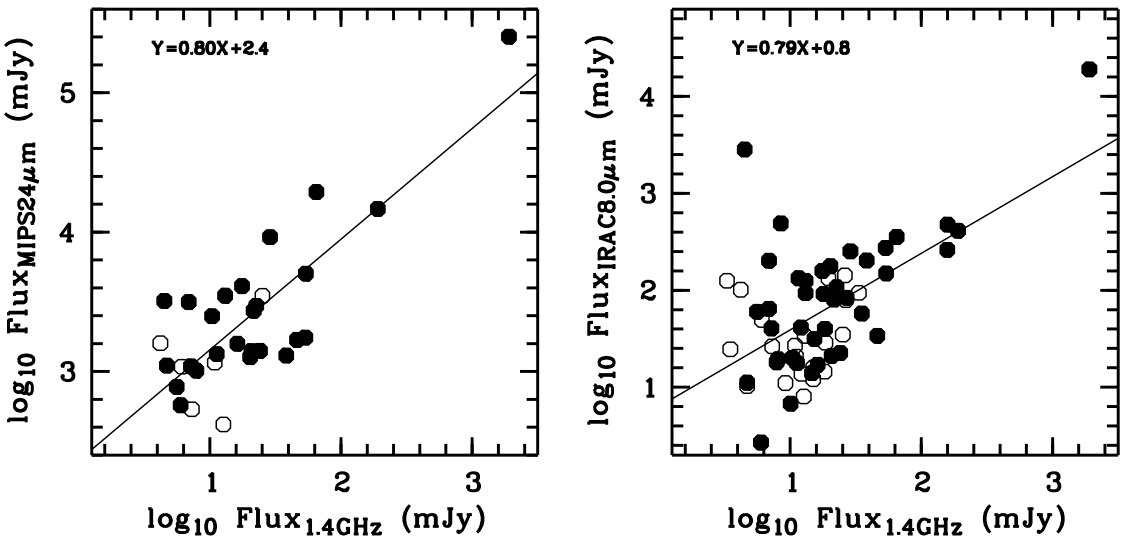

Fig. 13.— Left panel: MIPS 24 μm vs. NVSS 1.4 GHz integrated fluxes for 31 PNs. Right panel: IRAC 8.0 μm vs. NVSS 1.4 GHz integrated fluxes for 61 PNs. The solid line represents a linear fitting. The open and filled circles denote the MASH and known PNs, respectively.

Table 1. Spitzer observations of the GLIMPSE 3D PNs.

Objects[a]	Coordinate (J2000.0)		Flux (mJy)[b]				
	R.A.	Dec.	3.6μm	4.5μm	5.8μm	8.0μm	24μm
MASH PNs							
PNG 000.4 + 04.4 I t	17 29 52.4	-26 11 13	3.05	5.83	3.65	20.66	···
PNG 001.0 + 02.2 I l	17 39 11.3	-26 52 20	7.24	8.42	10.67	18.93	210.98
PNG 001.1 + 02.2 II t	17 39 49.7	-26 48 45	7.24	9.70	11.08	12.91	···
PNG 001.2 + 02.8 I l	17 37 30.3	-26 21 44	7.07	5.94	5.94	13.71	60.96
PNG 001.5 + 03.1 I t	17 37 16.5	-25 59 38	8.80	10.94	11.92	24.66	···
PNG 001.5 − 02.8 I p	18 00 22.4	-29 04 39	6.97	8.54	13.50	19.44	···
PNG 001.7 + 03.6 I t	17 35 47.4	-25 27 43	7.05	6.29	5.64	12.18	325.37
PNG 001.7 − 02.6 I t	18 00 00.6	-28 46 27	4.87	4.33	2.75	6.81	614.37
PNG 002.1 + 02.6 I t	17 40 30.7	-25 44 40	13.00	9.03	7.60	8.00	148.69
PNG 002.2 + 01.7 I p	17 44 01.7	-26 05 45	5.13	6.76	5.09	10.92	139.36
PNG 002.3 + 01.7 I t	17 44 35.4	-26 03 36	5.44	5.70	6.41	12.06	79.72
PNG 002.3 − 01.7 I p	17 57 43.5	-27 50 44	25.22	26.17	20.87	102.57	881.18
PNG 002.5 + 02.0 I l	17 43 39.5	-25 38 17	6.71	8.78	8.87	16.48	150.33
PNG 002.7 + 01.7 I t	17 45 18.9	-25 42 05	18.97	12.50	8.46	7.78	72.56
PNG 002.9 − 02.7 I l	18 03 05.1	-27 46 44	25.00	24.81	41.73	93.72	357.81
PNG 003.1 − 01.6 I t	17 59 26.1	-27 06 34	56.14	44.92	48.07	97.62	345.64
PNG 003.4 − 01.8 I t	18 00 42.3	-26 53 37	11.36	9.14	7.39	14.35	115.73
PNG 004.2 − 02.5 I t	18 05 20.1	-26 31 45	6.49	8.23	4.46	13.96	429.43
PNG 004.3 + 01.8*a* I t	17 48 33.0	-24 17 36	5.27	5.41	4.67	10.17	367.37
PNG 005.2 − 01.6 I t	18 03 52.4	-25 16 59	···	27.60	···	39.39	162.06
PNG 005.8 + 02.2*a* II t	17 50 20.7	-22 48 24	12.29	16.55	23.97	65.31	···
PNG 006.0 + 01.2 I p	17 54 44.8	-23 09 07	13.05	12.86	10.17	10.89	500.87
PNG 006.1 + 01.5 I t	17 53 45.3	-22 54 01	11.03	22.42	14.77	34.89	3487.26
PNG 006.1 − 02.1 I t	18 07 40.9	-24 39 18	1.56	2.73	3.50	10.57	225.94
PNG 006.9 + 01.5 II t	17 55 36.7	-22 12 47	5.04	6.19	4.28	5.02	···
PNG 007.5 − 02.4 I t	18 11 40.6	-23 37 16	4.57	9.57	5.03	11.03	···
PNG 007.8 + 01.2 II l	17 58 33.9	-21 35 15	2.85	4.23	2.66	6.84	···
PNG 009.4 − 01.2 I t	18 11 10.6	-21 23 14	12.77	13.86	13.02	28.76	···
PNG 009.7 − 01.1 I p	18 11 41.3	-21 02 29	1.30	2.02	5.61	24.15	···
PNG 009.8 − 01.1 I t	18 11 39.0	-21 00 44	13.81	27.93	56.37	125.31	···
PNG 010.0 − 01.5 I t	18 13 35.4	-20 57 05	24.17	42.96	60.90	93.89	···
PNG 010.2 + 02.4 I l	17 59 05.1	-18 53 22	3.85	4.47	4.32	7.25	···
PNG 010.2 + 02.7 I t	17 58 14.4	-18 41 26	3.33	12.20	6.82	14.45	···
PNG 010.6 + 02.4 II t	18 00 08.2	-18 34 34	4.64	4.64	5.82	9.07	···
PNG 010.7 − 02.3 II t	18 18 04.4	-20 44 14	11.56	15.48	9.18	17.66	···
PNG 011.0 + 01.4 I t	18 04 29.2	-18 42 41	26.03	23.77	24.40	33.77	···
PNG 011.0 − 02.9 I t	18 20 53.8	-20 48 12	6.72	9.02	5.89	15.96	···
PNG 017.6 + 02.6 I t	18 13 33.7	-12 20 48	6.86	13.51	8.80	79.05	···
PNG 019.2 − 01.6 II t	18 31 53.0	-12 56 14	4.30	8.79	4.48	12.11	···
PNG 024.2 + 01.8 II t	18 28 48.0	-06 52 00	1.88	2.72	1.80	6.78	···
PNG 025.6 + 02.8 II t	18 27 57.4	-05 10 23	2.15	3.17	2.35	10.27	···
PNG 029.0 + 02.2 II t	18 36 10.7	-02 27 14	4.41	8.82	4.94	13.73	···
PNG 029.2 − 01.8 I t	18 51 12.1	-04 08 55	2.93	3.83	4.33	8.23:	···
PNG 029.4 − 02.3 II t	18 53 30.6	-04 14 09	4.35	3.53	1.66	4.38	···

Table 1—Continued

Objects[a]	Coordinate (J2000.0)		Flux (mJy)[b]				
	R.A.	Dec.	3.6μm	4.5μm	5.8μm	8.0μm	24μm
PNG 030.2 + 01.5 II t	18 41 04.5	-01 40 49	2.28	4.18	4.30	7.72	···
PNG 031.0 − 02.1 II t	18 55 34.6	02 40 27	4.11	4.16	3.94	7.60	···
PNG 329.8 − 03.0 I t	16 17 19.8	-54 45 12	3.96	···	9.76	···	···
PNG 330.1 + 02.6 II t	15 54 08.9	-50 22 39	6.66	8.07	12.22	41.53	···
PNG 330.7 + 02.7 I t	15 56 33.0	-49 55 55	86.96	94.47	90.62	107.24	···
PNG 334.0 + 02.4 II t	16 12 40.6	-47 50 14	3.61	4.89	5.89	16.80	···
PNG 334.4 + 02.3 II t	16 14 52.3	-47 42 11	3.61	9.11	4.73	11.00	···
PNG 335.4 − 01.9 I t	16 37 44.9	-49 57 50	14.51	19.49	13.91	47.59	···
PNG 335.8 − 01.6 II p	16 38 01.7	-49 27 18	11.69	17.41	61.41	199.82	···
PNG 335.9 − 01.3 II p	16 37 14.2	-49 11 16	20.36	25.59	61.77	257.63	···
PNG 341.7 + 02.6 I t	16 42 18.6	-42 14 45	6.51	9.40	18.16	43.94:	···
PNG 341.9 − 02.8 II t	17 06 25.2	-45 27 04	2.78	5.11	2.99	8.86	···
PNG 342.1 − 02.0 II t	17 03 24.0	-44 50 30	1.50	3.25	1.39	2.90	···
PNG 344.0 + 02.5 II t	16 50 20.2	-40 30 03	1.84	2.83	2.46	7.75	···
PNG 344.4 + 01.8 II l	16 54 43.2	-40 41 47	3.10	4.12	4.68	10.85	···
PNG 344.8 − 02.6 II t	17 15 15.9	-43 03 54	3.55	5.17	3.73	5.91	···
PNG 345.8 + 02.4 II t	16 56 40.1	-39 12 37	1.46	2.55	2.52	8.34	···
PNG 345.8 + 02.7 I t	16 55 51.9	-39 00 21	1.83	2.63	5.16	10.68	···
PNG 349.6 − 02.1 II t	17 27 36.8	-38 51 09	1.81	2.16	2.24	2.63	···
PNG 350.4 + 02.0 I l	17 12 34.0	-35 43 20	12.97	13.54	10.73	33.82	···
PNG 350.8 + 01.7 II p	17 14 49.8	-35 35 40	1.19	1.49	8.54	133.01	···
PNG 350.8 − 03.0 I t	17 34 52.8	-38 17 19	1.59	1.11	1.03	3.28	···
PNG 355.0 + 02.6 I t	17 22 40.8	-31 39 55	21.79	26.77	39.78	142.29	···
PNG 355.2 − 02.0 I t	17 41 59.1	-34 05 34	27.14	34.66	35.32	49.19	···
PNG 355.8 + 01.7 II t	17 28 31.1	-31 32 09	4.40	···	7.17	···	···
PNG 356.0 + 02.8 I t	17 24 58.3	-30 43 04	5.94	7.50	9.13	17.09	652.38
PNG 356.0 − 01.8 I t	17 43 07.2	-33 15 54	4.21	6.83	3.81	9.33	556.13
PNG 356.1 − 02.7 I t	17 47 04.8	-33 41 03	1.14	2.72	1.97	8.19	451.52
PNG 356.2 + 02.5 I t	17 26 23.6	-30 45 39	4.89	5.78	4.94	8.01	416.23
PNG 356.2 + 02.7 II t	17 25 33.4	-30 33 57	1.67	2.04	2.15	3.89	···
PNG 356.3 − 02.6 II t	17 47 27.5	-33 26 38	18.71	12.06	8.24	9.03	···
PNG 356.5 − 01.8 I p	17 44 28.0	-32 52 11	31.66	31.63	30.72	49.38	1082.72
PNG 356.6 + 02.3 I t	17 28 14.2	-30 32 14	3.09	3.94	4.06	7.76	149.27
PNG 357.3 − 02.0 I t	17 47 28.5	-32 15 46	14.53	15.94	33.35	101.19	1593.93
PNG 357.5 − 02.4 I t	17 49 37.9	-32 16 28	7.22	9.47	4.76	26.35	535.03
PNG 357.8 + 01.6 I t	17 34 01.7	-29 54 35	47.99	···	20.90	···	620.67
PNG 357.9 + 01.7 I l	17 33 38.4	-29 45 30	2.27	3.46	3.74	11.21	420.71
PNG 358.0 − 02.4 I t	17 50 48.5	-31 52 27	13.79	10.62	9.56	15.57	535.93
PNG 358.1 + 02.3 I p	17 31 58.3	-29 15 01	50.84	66.73	77.74	93.80	176.68
PNG 358.4 + 02.1 I l	17 33 40.5	-29 08 34	9.04	7.50	3.90	6.89	391.82
PNG 358.7 − 02.5 I t	17 52 36.5	-31 16 27	56.60	33.18	25.54	20.99	85.54
PNG 359.2 − 02.4 I t	17 53 39.8	-30 51 25	2.38	2.81	1.87	5.62	149.90
PNG 359.4 + 02.3*a* I t	17 35 12.0	-28 09 31	4.47	4.85	6.67	10.41	187.65
PNG 359.6 + 04.3 I l	17 27 58.4	-26 53 45	3.76	4.15	4.55	6.86	···
PNG 359.7 + 02.0 I p	17 36 56.8	-28 04 42	13.71	17.60	17.79	26.90	1156.71

Table 1—Continued

Objects[a]	Coordinate (J2000.0)		Flux (mJy)[b]				
	R.A.	Dec.	3.6μm	4.5μm	5.8μm	8.0μm	24μm
PNG 359.8 + 03.5 I p	17 31 47.8	-27 09 19	8.58	8.10	9.78	20.26	···
Known PNs							
Al 2-B	17 27 47.06	-28 11 00.76	11.08	13.97	12.05	27.39	...
Al 2-E	17 30 14.40	-27 30 19.41	5.19	13.05	9.96	13.98	...
Al 2-F	17 30 30.43	-28 35 54.90	0.90	1.15	0.95	2.23	...
Al 2-G	17 32 22.67	-28 14 27.32	54.49	101.47	168.58	413.55	1251
Al 2-J	17 35 35.50	-27 24 06.50	2.43	4.45	1.58	2.69	573.0
Al 2-K	17 36 14.18	-28 00 46.33	10.03	12.42	13.49	22.52	419.0
Al 2-O	17 51 45.29	-32 03 03.90	63.01	91.83	135.67	202.92	1301
Al 2-R	17 53 36.46	-31 25 25.70	5.19	6.13	4.63	8.59	672.0
Bl 3-10	17 55 20.54	-29 57 36.13	8.11	10.15	7.78	11.16	1102
H 1-16	17 29 23.39	-26 26 05.00	17.61	...	29.20	...	...
H 1-17	17 29 40.59	-28 40 22.12	15.44	27.34	34.14	201.90	...
H 1-18	17 29 42.76	-29 32 50.30	14.54	19.73	36.62	158.30	4098
H 1-19	17 30 02.55	-27 59 17.54	23.83	24.21	38.19	133.18	...
H 1-20	17 30 43.82	-28 04 06.80	9.92	17.19	15.33	83.57	...
H 1-22	17 32 22.14	-37 57 23.80	7.40	12.65	10.31	40.00	...
H 1-29	17 44 13.82	-34 17 33.05	13.21	14.62	43.78	145.56	1264
H 1-31	17 45 32.10	-34 33 55.32	6.44	11.09	9.45	35.40	...
H 1-32	17 46 06.30	-34 03 45.40	15.60	20.59	15.41	65.04	4176
H 1-34	17 48 07.57	-22 46 47.33	16.46	17.60	61.30	221.53	5535
H 1-40	17 55 36.05	-30 33 32.30	18.78	30.10	48.53	489.98	> 9715
H 1-45	17 58 21.87	-28 14 52.30	1409.92	2133.31	6280.78	> 3754.65	1584
H 1-53	18 05 57.43	-26 29 42.00	3.65	5.36	8.00	40.50	1089
H 1-6	17 06 58.87	-42 41 09.75	22.33	28.51	29.57	72.79	...
H 1-7	17 10 27.39	-41 52 49.42	193.43	191.04	484.47	1380.74	...
H 2-10	17 27 32.85	-28 31 06.90	5.29	8.23	5.18	12.16	...
H 2-13	17 31 08.08	-30 10 28.00	5.57	9.77	5.78	20.05	1331
H 2-20	17 45 39.77	-25 40 00.04	45.43	50.08	43.73	93.53	3500
H 2-24	17 48 36.54	-24 16 34.80	1091.21	1512.34	3466.65	> 2831.43	3209
H 2-33	17 58 12.54	-31 07 51.10	4.23	5.57	3.36	19.49	...
HDW 8	17 31 47.47	-28 42 03.37	46.56	60.90	49.36	150.90	2297
Hb 4	17 41 52.76	-24 42 08.07	48.36	79.03	75.62	261.68	...
Hb 6	17 55 07.02	-21 44 39.98	95.71	153.35	111.41	412.57	14660
He 2-149	16 14 24.27	-54 47 38.82	2.47	4.24	2.21	10.40	...
He 2-153	16 17 14.43	-53 32 08.39	15.67	17.09	18.49	35.71	...
He 2-157	16 22 14.26	-53 40 54.09	8.60	12.99	10.68	45.39	...
He 2-169	16 34 13.33	-49 21 13.20	37.56	62.84	76.82	273.96	1750
He 2-250	17 34 54.71	-26 35 56.92	7.05	13.68	6.56	31.51	...
He 2-262	17 40 12.84	-26 44 21.90	10.11	14.91	9.75	22.58	1405
IC 4673	18 03 18.41	-27 06 22.61	16.03	46.52	17.74	137.92	...
IRAS 17218-3126	17 25 03.47	-31 28 38.50	4.58	9.66	4.90	27.24	1072
IRAS 18023-2513	18 05 25.51	-25 13 37.23	12.51	18.50	13.44	42.92	2445
JaFu 1	17 43 57.38	-26 11 53.98	4.46	6.41	6.25	11.72	79.0

Table 1—Continued

Objects[a]	Coordinate (J2000.0)		Flux (mJy)[b]				
	R.A.	Dec.	3.6μm	4.5μm	5.8μm	8.0μm	24μm
K 5-10	17 41 24.52	-26 03 53.40	29.97	34.83	35.71	60.05	776.0
K 5-13	17 43 39.44	-25 36 42.51	4.65	8.66	4.97	17.71	1335
K 5-16	17 45 28.31	-25 38 10.41	3.27	4.98	3.46	12.19	139.0
K 5-19	17 49 51.28	-23 27 44.27	4.46	8.29	4.72	10.76	715.0
K 6-12	17 47 17.80	-33 15 39.00	3.37	3.99	3.45	7.30	31.0
K 6-14	17 48 28.47	-24 41 25.07	8.26	9.59	7.53	21.04	1403
KFL 1	17 59 15.59	-30 02 47.15	4.05	5.94	3.22	6.98	...
KFL 2	18 00 59.92	-28 16 19.80	3.16	2.74	1.77	2.04	182.0
KFL 3	18 02 52.93	-31 23 58.49	...	1.51	...	3.33	...
KFL 4	18 02 51.67	-27 40 59.60	3.85	2.91	2.39	2.05	79.0
KFL 5	18 03 53.66	-29 51 21.89	31.81	56.71	85.26	225.22	...
M 1-27	17 46 45.45	-33 08 35.06	55.41	66.33	95.00	354.99	19390
M 1-31	17 52 41.44	-22 21 57.00	29.36	40.84	64.70	252.59	9210
M 1-35	18 03 39.30	-26 43 33.90	21.14	33.09	28.46	149.55	5039
M 1-41	18 09 29.90	-24 12 23.46	125.10	203.08	243.89	648.50	13670
M 2-21	17 58 09.58	-29 44 20.10	21.98	29.13	57.71	177.23	1269
M 2-23	18 01 42.64	-28 25 44.20	21.89	31.26	25.92	216.84	5688
M 2-26	18 03 11.41	-26 58 30.23	4.49	7.04	4.16	22.77	...
M 2-46	18 46 34.61	-08 28 02.10	14.45	16.14	44.14	125.17	...
M 3-10	17 27 20.19	-28 27 51.20	14.47	28.02	18.37	57.51	...
M 3-14	17 44 20.62	-34 06 40.60	12.62	19.91	24.61	107.50	2961
M 3-16	17 52 46.05	-30 49 34.42	6.41	10.85	8.32	15.67	531.0
M 3-19	17 58 19.34	-30 00 39.32	5.36	5.71	4.75	18.12	1014
M 3-20	17 59 19.35	-28 13 48.20	6.25	10.10	7.15	17.05	1581
M 3-22	18 02 19.24	-30 14 25.38	1.59	4.68	3.62	6.78	...
M 3-24	18 07 53.91	-25 24 02.71	5.27	9.28	7.05	37.26	1154
M 3-46	17 55 05.79	-31 12 16.03	7.79	8.29	7.16	18.76	140.0
M 3-47	17 57 43.37	-30 02 29.91	1.93	2.01	1.83	4.08	48.0
M 3-48	17 59 56.82	-31 54 27.46	6.58	5.35	5.54	8.23	...
M 3-8	17 24 52.15	-28 05 54.61	51.30	37.21	30.33	91.70	...
M 4-10	18 34 13.85	-13 12 24.70	9.75	16.31	12.76	41.27	...
M 4-4	17 28 50.29	-30 07 45.10	95.04	62.44	46.55	54.99	1120
MaC 1-10	18 09 12.88	-25 04 33.27	175.82	288.86	588.34	2076.00	$>$ 11518
MeWe 1-6	16 31 06.65	-50 26 38.08	5.53	9.86	10.40	12.51	...
Mz 2	16 14 32.42	-54 57 04.20	18.24	38.94	40.98	105.89	...
NGC 6302	17 13 44.21	-37 06 15.94	687.77	2174.08	3400.33	$>$19020.20	252810
NGC 6578	18 16 16.52	-20 27 02.67	306.55	295.80	253.76	475.52	...
PN 1824-1410	18 27 13.51	-14 08 34.70	25.70	43.09	33.55	31.72	...
Pe 1-15	18 46 24.49	-07 14 34.57	16.75	19.77	18.52	50.80	...
Pe 1-6	16 23 54.31	-46 42 15.28	6.78	10.91	4.59	28.84	...
Pe 2-10	17 53 37.22	-21 58 41.80	14.52	13.03	8.90	14.17	192.0
Pe 2-11	17 58 31.27	-27 37 05.80	13.14	20.84	22.13	27.21	...
Pe 2-12	18 01 10.30	-27 38 19.88	15.77	10.74	8.15	8.36	952.0
Sa 3-104	17 58 25.80	-29 20 49.00	57.38	114.46	208.25	584.52	2867
SaWe 2	17 27 00.19	-27 40 35.11	8.43	8.50	11.86	26.50	...

Table 1—Continued

Objects[a]	Coordinate (J2000.0)		Flux (mJy)[b]				
	R.A.	Dec.	3.6μm	4.5μm	5.8μm	8.0μm	24μm
ShWi 1	18 02 25.85	-29 25 05.40	0.62	0.77	0.75	2.28	...
Th 3-10	17 24 40.90	-30 51 59.60	14.71	26.43	26.18	80.20	2731
Th 3-11	17 24 26.33	-31 43 19.80	12.85	13.55	21.07	64.47	3148
Th 3-13	17 25 19.38	-29 40 42.00	23.17	36.26	77.98	361.50	$>$ 5871
Th 3-19	17 28 41.79	-28 27 19.32	5.43	7.32	6.24	16.86	...
Th 3-23	17 30 21.36	-29 10 12.70	13.28	27.72	22.96	33.99	1686
Th 3-24	17 30 51.35	-30 17 12.49	4.13	4.96	4.11	6.75	85.0
Th 3-25	17 30 46.81	-27 05 58.00	7.90	11.12	6.82	17.35	...
Th 3-26	17 31 09.29	-28 14 50.43	3.75	11.05	9.14	20.10	$>$ 2495
Th 3-33	17 35 48.12	-27 43 20.38	21.28	19.27	95.83	241.35	3545
Th 4-3	17 48 37.39	-22 16 48.79	4.50	5.31	5.71	17.06	1942
Th 4-7	17 52 22.57	-21 51 13.43	2.93	6.63	8.93	14.51	695.0
Th 4-9	17 56 00.60	-19 29 26.70	37.00	70.33	118.73	375.53	...
Vd 1-5	16 51 33.58	-40 02 56.01	1.77	3.95	2.22	4.87	...

[a]The 'I' and 'II' after the PN designations represent the MASH I and MASH II, respectively. The 't', 'l', and 'p' represent true, likely, and possible PNs, respectively, as assigned in the MASH I&II catalogue.

[b]The colon represents uncertain detection. For saturating sources, the lower limits of fluxes are given.

Table 2. Flux measurements from the AKARI point source catalogue

Objects	IRC flux (Jy)		FIS flux (Jy)			
	9μm	18μm	65μm	90μm	140μm	160μm
MASH PNs						
PNG 000.4 + 04.4	···	0.943	···	···	···	···
PNG 001.5 + 03.1	···	0.754	2.396:	2.963	···	···
PNG 001.7 + 03.6	···	···	0.932:	0.94	0.491:	0.611:
PNG 001.7 − 02.6	···	···	1.173:	1.77	···	···
PNG 002.3 − 01.7	···	0.944	···	···	···	···
PNG 002.9 − 02.7	0.169	0.37	···	···	···	···
PNG 003.1 − 01.6	···	···	4.048:	6.575	4.924:	6.003:
PNG 007.5 − 02.4	···	0.705	···	···	···	···
PNG 007.8 + 01.2	···	0.253	···	···	···	···
PNG 009.4 − 01.2	···	1.388	···	···	···	···
PNG 009.8 − 01.1	···	0.554	4.035:	4.696	11.948	···
PNG 010.2 + 02.4	···	···	3.122:	1.417	6.395	2.206:
PNG 010.2 + 02.7	···	0.844	···	···	···	···
PNG 010.6 + 02.4	···	0.5	1.855:	1.416	4.593:	···
PNG 010.7 − 02.3	···	0.55	4.957:	3.122:	6.939	3.708:
PNG 011.0 + 01.4	···	···	0.686:	3.709	8.454	9.32:
PNG 011.0 − 02.9	···	···	···	2.609	···	5.206:
PNG 017.6 + 02.6	···	1.864	···	···	···	···
PNG 024.2 + 01.8	···	0.249	0.794:	1.249	···	···
PNG 025.6 + 02.8	···	0.693	···	···	···	···
PNG 029.0 + 02.2	···	0.925	···	···	···	···
PNG 030.2 + 01.5	···	0.204	···	···	···	···
PNG 329.8 − 03.0	···	···	1.918	1.541	4.299:	3.389:
PNG 330.1 + 02.6	···	0.863	···	···	···	···
PNG 334.0 + 02.4	···	0.145	3.40:	1.749	···	0.261:
PNG 334.4 + 02.3	···	0.424	0.62:	1.664	1.425:	···
PNG 335.4 − 01.9	0.192	0.712	···	7.93	3.24	4.735
PNG 335.8 − 01.6	0.264	0.949	···	···	···	···
PNG 335.9 − 01.3	0.485	5.498	10.406	8.67	3.272:	5.604:
PNG 341.9 − 02.8	···	0.337	···	···	···	···
PNG 344.0 + 02.5	···	0.426	···	···	···	···
PNG 350.4 + 02.0	···	1.655	···	···	···	···
PNG 350.8 + 01.7	···	2.48	5.81:	5.519	13.89	1.725:
PNG 355.0 + 02.6	0.231	3.144	···	···	···	···
PNG 355.2 − 02.0	···	0.362	···	···	···	···
PNG 356.0 + 02.8	···	0.584	···	···	···	···
PNG 356.5 − 01.8	···	0.886	···	···	···	···
PNG 357.3 − 02.0	···	1.199	9.077	3.472	2.255:	···
PNG 357.8 + 01.6	···	0.631	···	···	···	···
PNG 357.9 + 01.7	···	···	0.671:	2.793	10.986:	9.99:
PNG 358.0 − 02.4	···	0.50	···	···	···	···
PNG 358.1 + 02.3	···	0.173	···	···	···	···
PNG 359.7 + 02.0	···	1.012	···	···	···	···
PNG 359.8 + 03.5	···	0.881	···	···	···	···

Table 2—Continued

Objects	IRC flux (Jy)		FIS flux (Jy)			
	9μm	18μm	65μm	90μm	140μm	160μm
Known PNs						
Al 2-E	...	0.873	1.227:	2.023	...	0.023:
Al 2-G	...	1.013	...	...	...	...
Al 2-O	0.241	0.582	...	...	...	...
Al 2-R	...	0.306	...	...	...	...
Bl 3-10	...	0.357	...	...	...	...
H 1-16	0.272	...	...	...	...	...
H 1-17	0.617	6.259	...	...	...	...
H 1-18	0.336	2.667	...	...	...	...
H 1-19	0.185	2.864	5.167	4.579	...	1.333:
H 1-20	...	1.924	3.73	3.436	...	...
H 1-22	...	1.517	...	...	...	...
H 1-29	0.174	...	...	...	...	...
H 1-32	0.266	...	...	...	...	...
H 1-34	0.352	...	...	...	...	...
H 1-40	1.255	10.494	8.689	7.947	3.121:	2.002:
H 1-45	5.230	2.443	...	...	...	...
H 1-53	...	0.651	...	...	...	...
H 1-6	...	0.670	...	...	...	...
H 1-7	1.892	13.029	...	42.37:	33.76	10.955:
H 2-10	...	1.045	...	...	...	...
H 2-13	...	1.052	...	...	...	...
H 2-20	...	1.474	...	...	...	...
H 2-24	...	3.535	...	...	...	...
H 2-33	...	0.393	1.633:	2.283	...	...
HDW 8	0.728	2.139	...	...	...	...
Hb 4	...	5.449	13.541	14.269	0.952:	1.287:
Hb 6	1.144	...	20.768:	14.246	6.261:	2.636:
He 2-149	...	0.542	...	1.020	...	...
He 2-153	...	0.298	...	...	...	...
He 2-157	...	1.951	2.612:	2.420	...	0.963:
He 2-169	0.338	1.697	12.73	11.83	14.61	18.50:
He 2-250	...	0.728	2.625	3.213	...	0.965:
He 2-262	...	1.082	...	...	...	...
IC 4673	...	3.057	9.901:	9.916	6.940:	6.241:
IRAS 17218-3126	...	0.533	...	...	...	...
IRAS 18023-2513	0.156	1.668	1.296:	5.988	1.724:	...
K 5-10	...	0.693	...	...	....	...
K 5-13	...	0.658	...	...	...	...
K 6-14	...	0.627	...	...	...	...
KFL 5	0.468	0.800	...	...	...	...
M 1-27	0.446	...	...	...	...	...
M 1-31	0.435	5.727	...	...	...	...
M 1-35	0.514	3.572	...	...	...	...

Table 2—Continued

Objects	IRC flux (Jy)		FIS flux (Jy)			
	9μm	18μm	65μm	90μm	140μm	160μm
M 1-41	1.320	5.912	...	...	...	...
M 2-21	0.305	0.789	...	...	...	...
M 2-23	...	6.155	...	...	...	...
M 2-26	...	0.398	...	...	...	...
M 2-46	0.111	0.455	2.976	4.938	2.008:	2.894:
M 3-10	0.311	2.611	2.650:	2.658	...	2.107:
M 3-14	0.344	1.889	...	...	...	...
M 3-19	...	0.800	...	...	...	...
M 3-20	0.091	...	1.786:	1.353	...	...
M 3-22	...	0.451	1.334:	1.319	0.941:	0.998:
M 3-24	...	0.887	5.998	3.891	0.071:	...
M 3-48	...	...	0.104:	0.419	...	...
M 3-8	0.297	...	...	...	...	...
M 4-10	...	1.920	...	...	...	...
M 4-4	0.088	...	...	...	...	...
MaC 1-10	2.791	12.058	...	...	...	...
Mz 2	...	1.763	6.39	7.386:	2.8:	0.136:
NGC 6302	...	156.07	670.18	304.59	188.33	201.675
NGC 6578	1.357	...	20.146	26.884:	10.368:	4.589:
Pe 1-15	0.079	0.722	2.534	2.029	...	...
Pe 1-6	0.191	0.823	...	4.576	...	...
Sa 3-104	0.866	2.315	...	...	...	...
SaWe 2	...	...	0.562	2.44:	1.572	...
Th 3-10	0.152	1.635	...	...	...	...
Th 3-11	...	1.542	...	...	...	...
Th 3-13	...	4.774	8.348	2.537:	...	...
Th 3-19	...	0.967	...	...	...	...
Th 3-23	...	0.847	...	...	...	...
Th 3-25	...	0.841	0.043:	1.042	0.528:	2.846:
Th 3-26	...	...	2.622:	2.337	...	...
Th 3-33	...	2.064	...	...	...	...
Th 4-3	...	1.015	1.110:	1.217	0.433:	...
Th 4-7	...	0.276	...	...	...	...
Th 4-9	0.595	1.13	...	...	...	...
Vd 1-5	...	0.139	...	...	...	...

Table 3. Other flux measurements

Object	DENIS I (mag)	DENIS J (mag)	DENIS K (mag)	2MASS J (mag)	2MASS H (mag)	2MASS K (mag)	*MSX* 8.28 μm (Jy)	*MSX* 12.13 μm (Jy)	*MSX* 14.65 μm (Jy)	*MSX* 21.3 μm (Jy)	*IRAS* 12 μm (Jy)	*IRAS* 25 μm (Jy)	*IRAS* 60 μm (Jy)	*IRAS* 100 μm (Jy)	NVSS 1.4 GHz (mJy)
MASH PNs															
PNG 000.4 + 04.4	16.997	14.946	...	15.166	14.352	13.686	0.070	...	0.654	1.133	0.383	2.026	3.835	10.490	11.1
PNG 001.0 + 02.2	15.926	14.312	...	14.347	13.748	13.336	...	...	...	...	...	...	...	...	...
PNG 001.1 + 02.2	16.717	...	...	15.108	13.583	13.172	...	...	...	...	...	...	...	...	...
PNG 001.5 − 02.8	...	...	...	14.019	13.064	12.812	...	...	...	...	...	...	...	...	...
PNG 001.5 + 03.1	...	...	...	14.231	13.155	12.722	...	...	...	...	< 2.302	1.825	4.806	< 18.230	3.5
PNG 002.3 − 01.7	15.180	...	11.971	13.745	13.020	12.089	0.191	...	...	1.576	...	...	...	...	...
PNG 002.5 + 02.0	...	...	...	14.549	13.550	13.095	...	...	...	...	...	...	...	...	...
PNG 002.9 − 02.7	14.010	12.097	10.920	12.234	11.374	11.023	0.139	...	...	2.148:	...	...	...	...	...
PNG 005.8 + 02.2a	16.302	14.584	...	15.203	14.055	13.744	...	...	...	...	...	...	...	...	...
PNG 006.0 + 01.2	16.869	14.576	...	14.558	13.633	12.658	...	...	...	...	...	...	...	...	...
PNG 006.1 + 01.5	14.389	13.384	12.725	13.489	12.948	12.740	0.111	...	0.978	2.369	< 2.092	2.910	5.425	46.310	25.2
PNG 007.5 − 02.4	...	...	...	...	...	...	...	...	...	...	< 1.391	1.527	< 17.79	< 169.50	9.2
PNG 009.4 − 01.2	...	14.395	12.476	14.345	13.129	12.518	...	...	...	...	...	...	...	...	18.6
PNG 009.8 − 01.1	...	15.358	13.422	14.978	13.894	13.178	...	...	...	...	...	...	...	...	3.3
PNG 010.0 − 01.5	18.170	14.760	13.256	14.890	13.583	13.205	...	...	...	...	...	...	...	...	33.4
PNG 010.2 + 02.7	17.077	15.329	...	15.356	14.229	13.857	...	...	...	...	...	...	...	...	18.3
PNG 011.0 − 02.9	16.046	14.264	13.058	14.257	13.552	13.247	...	...	...	...	< 0.362	0.670	3.112	< 88.61	15.0
PNG 017.6 + 02.6	...	15.578	13.567	16.076	14.196	13.834	0.186	1.155	1.876	2.779	...	...	...	...	26.6
PNG 019.2 − 01.6	...	...	...	...	...	...	...	...	...	...	< 1.521	1.667	4.330	< 348.10	15.0
PNG 025.6 + 02.8	16.864	14.906	13.759	15.036	14.603	13.764	...	...	...	...	< 0.260	1.330	< 1.289	< 17.360	4.7
PNG 029.0 + 02.2	16.634	14.393	13.101	14.434	14.091	13.215	...	...	...	...	< 1.259	1.611	< 11.460	< 136.900	12.2
PNG 029.2 − 01.8	...	15.386	...	15.481	14.294	13.907	...	...	...	...	...	...	...	...	...
PNG 329.8 − 03.0	16.678	15.359	13.854	15.430	14.756	14.548	...	...	...	...	...	...	...	...	...
PNG 330.1 + 02.6	16.526	14.374	13.015	14.631	14.195	13.151	...	...	...	...	< 0.250	1.994	3.156	< 21.550	...
PNG 334.0 + 02.4	17.184	15.131	...	15.258	14.549	13.851	...	...	...	...	...	...	...	...	...
PNG 334.4 + 02.3	17.696	15.548	...	15.990	14.377	14.564	...	...	...	...	...	...	...	...	...
PNG 335.4 − 01.9	17.343	14.886	...	14.351	13.338	12.852	0.169	...	0.719	...	< 1.728	0.979	7.515	< 331.200	...
PNG 335.8 − 01.6	...	...	...	14.309	13.719	13.479	0.218	...	0.588	...	0.560	1.730	< 49.04	< 482.200	...
PNG 335.9 − 01.3	15.342	13.275	11.782	13.275	12.574	11.894	0.364	0.784	1.415	8.175	...	...	...	...	...
PNG 341.7 + 02.6	...	14.825	13.346	14.864	13.691	13.248	...	...	...	...	...	...	...	...	...
PNG 341.9 − 02.8	...	...	...	15.907	14.790	14.090	...	...	...	...	...	...	...	...	...
PNG 344.0 + 02.5	17.194	15.144	...	15.570	14.878	14.510	...	...	...	...	...	...	...	...	...
PNG 344.4 + 01.8	...	...	...	15.101	14.422	14.052	...	...	...	...	...	...	...	...	...
PNG 345.8 + 02.4	...	...	...	16.082	15.622	14.635	...	...	...	...	...	...	...	...	...
PNG 345.8 + 02.7	16.993	15.674	...	15.770	15.365	15.392	...	...	...	...	...	...	...	...	...
PNG 350.4 + 02.0	...	14.825	13.346	15.038	14.669	14.128	...	...	...	...	< 1.867	3.298	6.299	< 154.200	12.9
PNG 350.8 + 01.7	...	14.576	12.408	14.749	13.838	12.593	0.139	0.871	1.221	2.618	< 1.731	3.715	8.260	< 188.900	19.6
PNG 355.0 + 02.6	...	13.742	11.745	14.230	13.480	12.306	0.217	...	2.062	4.172	...	...	...	...	26.1
PNG 355.8 + 01.7	...	...	...	...	...	...	...	...	...	...	<2.859	1.214	< 5.664	< 74.050	14.4
PNG 356.0 + 02.8	...	14.466	13.028	14.757	13.634	13.080	...	...	...	...	...	...	...	...	...
PNG 356.2 + 02.5	...	13.929	12.156	14.491	13.381	13.440	...	...	...	...	...	...	...	...	12.7
PNG 356.5 − 01.8	16.970	13.421	11.720	13.580	12.246	11.616	...	...	...	...	< 3.744	1.921	< 6.375	< 344.600	6.1
PNG 357.3 − 02.0	...	...	12.756	14.028	13.008	12.739	...	...	...	...	...	...	...	...	4.2
PNG 357.5 − 02.4	17.322	14.193	12.736	14.231	13.044	12.477	...	...	...	...	...	...	...	...	7.3
PNG 358.1 + 02.3	...	...	...	13.811	12.518	11.313	...	...	...	...	...	...	...	...	...
PNG 359.7 + 02.0	17.114	13.916	12.302	14.219	12.963	12.448	...	...	...	...	...	...	...	...	10.9
KnownPNs															

Table 3—Continued

Object	DENIS I (mag)	DENIS J (mag)	DENIS K (mag)	2MASS J (mag)	2MASS H (mag)	2MASS K (mag)	*MSX* 8.28 μm (Jy)	*MSX* 12.13 μm (Jy)	*MSX* 14.65 μm (Jy)	*MSX* 21.3 μm (Jy)	*IRAS* 12 μm (Jy)	*IRAS* 25 μm (Jy)	*IRAS* 60 μm (Jy)	*IRAS* 100 μm (Jy)	NVSS 1.4 GHz (mJy)
Al 2-E	...	...	...	...	...	...	...	...	...	...	< 2.42	2.3	3.65	< 15.54	14.7
Al 2-G	13.967	13.25	11.802	16.281	14.133	11.886	...	...	...	...	...	...	...	...	...
Al 2-J	...	...	...	...	...	...	...	...	...	...	1.63	1.14	< 1.84	< 22.03	6
Al 2-O	12.712	11.73	10.84	14.59	12.608	10.671	...	...	...	...	< 2.29	1.37	3.83	< 103.9	38.3
Bl 3-10	...	...	...	...	...	...	...	...	...	...	1.67	1.74	< 15.2	< 84.85	4.7
H 1-16	13.142	12.547	11.638	15.367	12.893	11.662	0.218	...	1.971	3.74	0.682	5.95	5.13	< 10.3	...
H 1-17	13.08	12.679	11.745	15.067	12.71	11.69	0.465	1.519	3.147	10.28	1.45	11.31	6.19	< 33.88	6.9
H 1-18	13.634	13.292	12.238	15.693	13.487	12.451	...	...	...	...	< 2.2	5.39	6.59	< 35.69	17.6
H 1-19	12.429	11.492	11.047	14.634	12.359	10.946	0.145	1.452	0.953	4.994	< 1.97	6.17	6.5	< 22.02	11.6
H 1-20	13.704	13.502	12.445	...	...	...	...	...	...	...	< 2.7	3.7	5.46	< 20.38	26.9
H 1-22	13.94	13.652	12.647	15.545	13.72	12.415	...	...	...	...	< 1.45	3.35	4.96	< 137.4	18.4
H 1-29	13.542	13.104	12.339	14.901	13.481	12.425	...	...	...	...	...	...	...	...	...
H 1-31	13.274	12.88	12.825	...	...	...	...	...	...	...	< 1.57	3.26	1.27	< 11.26	...
H 1-32	12.841	12.481	11.861	...	...	...	0.19	...	1.562	4.376	0.73	5.22	1.81	< 11.24	...
H 1-34	12.805	11.975	11.625	...	...	...	0.309	...	0.921	5.346	< 0.66	7.85	13.26	< 16.48	...
H 1-40	12.705	12.369	11.579	14.461	12.777	11.57	1.098	2.103	4.601	16.28	2.38	18.45	11.91	< 73.48	8.5
H 1-45	10.518	8.399	6.697	...	...	...	4.832	5.791	3.297	2.025	...	...	...	...	...
H 1-53	14.109	13.747	12.893	...	...	...	0.104	...	1.076	2.105	...	...	...	...	7.2
H 1-7	...	...	...	...	...	...	1.811	2.527	8.401	17.44	3.26	25.85	58.81	33.18	...
H 2-10	14.13	13.054	12.953	...	...	...	...	...	...	...	...	...	...	...	...
H 2-20	13.694	11.876	11.308	...	...	...	0.135	...	...	3.029	...	...	...	...	13.1
H 2-24	10.3	8.276	6.944	13.634	10.171	6.929	4.156	3.943	3.993	3.103	...	...	...	...	4.5
H 2-33	...	...	...	...	...	...	...	...	...	...	0.76	1.1	2.81	<59.86	8.1
HDW 8	...	...	...	...	...	...	0.392	...	1.572	2.581	...	...	...	...	...
Hb 4	12.738	12.466	11.601	14.402	12.606	11.252	...	...	...	...	1.34	10.30	<20.85	12.78	157.6
Hb 6	...	...	...	...	...	...	1.110	0.990:	7.978	15.08	1.58	22.49	27.36	<21.24	190.5
He 2-149	14.648	14.543	13.849	15.551	...	13.475	...	...	...	...	< 0.37	0.89	2.17	< 114.7	...
He 2-157	13.395	13.22	12.365	14.554	13.198	12.32	...	...	...	...	< 2.81	4.1	3.2	< 66.2	...
He 2-169	13.045	12.157	11.773	15.217	13.024	11.734	0.280	...	1.538	2.545:	<0.87	3.18	10.02	<390.1	53.4
He 2-250	...	...	...	...	...	...	0.121	...	1.125	...	< 2.01	2.01	< 4.51	16.15	15.3
He 2-262	13.779	12.632	12.55	15.581	13.647	12.619	...	...	...	...	2.19	3.0	< 2.51	< 27.07	24.1
IC 4673	...	...	...	...	...	...	0.335	...	1.957	4.015:	<4.80	7.82	<14.11	<44.73	...
IRAS 18023-2513	...	...	...	...	...	...	...	...	...	...	< 18.6	< 11.3	8.41	< 463	...
K 5-10	14.055	12.769	12.605	...	...	...	...	...	...	...	...	...	...	...	5.6
K 5-13	13.736	12.743	12.26	...	...	...	...	...	...	...	...	...	...	...	11.3
K 6-14	11.861	10.336	9.744	13.431	11.758	9.665	...	...	...	...	...	...	...	...	20.7
KFL 1	13.567	12.956	12.724	...	...	...	...	...	...	...	...	...	...	...	...
KFL 2	13.642	12.886	12.605	...	...	...	...	...	...	...	...	...	...	...	...
KFL 4	13.578	12.879	12.661	14.96	13.742	...	...	...	...	...	...	...	...	...	...
KFL 5	13.083	12.47	11.867	...	...	...	0.402	...	0.666	...	...	...	...	...	...
M 1-27	11.681	11.344	10.812	12.805	11.586	10.787	0.388	2.214	2.751	18.19	1.57	23.4	20.43	<187	64.9
M 1-31	12.751	12.509	11.495	14.342	12.455	11.507	0.419	0.792:	3.095	8.135	1.17	11.68	11.07	<34.90	28.8
M 1-35	13.151	12.99	11.869	14.637	12.915	11.718	0.458	...	3.393	4.048	1.4	7.25	14.05	< 154.5	54
M 1-41	14.181	13.999	12.369	...	...	...	...	...	...	...	3.27	10.74	38.18	<238.6	...
M 2-21	13.2	13.079	12.016	...	...	...	0.232	0.711	0.834	...	1.02	1.51	< 7.78	< 99.13	20.3
M 2-23	12.131	12.1	11.342	...	...	...	0.726	1.382	3.302	8.215	1.93	9.31	0.64	< 126.7	...
M 2-46	14.378	14.218	13.304	15.183	14.152	13.027	...	...	...	...	<0.38	0.98	4.56	10.81	13.1
M 3-10	13.175	12.97	12.064	14.705	13.01	12.103	0.179	...	1.402	3.346	< 0.6	5.11	4.27	< 16.23	35.2
M 3-14	13.831	13.153	12.407	15.324	13.315	12.555	0.23	1.305	1.68	2.502	< 4.43	3.31	7.33	< 13.69	22.6

Table 3—Continued

	DENIS			2MASS			*MSX*				*IRAS*				NVSS
	I	J	K	J	H	K	8.28 μm	12.13 μm	14.65 μm	21.3 μm	12 μm	25 μm	60 μm	100 μm	1.4 GHz
Object	(mag)	(mag)	(mag)	(mag)	(mag)	(mag)	(Jy)	(Jy)	(Jy)	(Jy)	(Jy)	(Jy)	(Jy)	(Jy)	(mJy)
M 3-16	...	...	...	...	...	...	...	...	...	...	< 2.6	0.88	2.42	< 45.58	...
M 3-19	12.154	11.176	10.921	...	...	...	...	...	...	...	< 4.44	1.47	5.09	< 63.03	7.9
M 3-20	13.674	13.512	12.756	...	...	...	...	...	...	...	...	...	...	...	16.2
M 3-22	...	...	...	...	...	...	...	...	...	...	< 5.37	2.34	1.81	< 69.59	10.1
M 3-47	14.043	13.356	13.043	...	...	...	...	...	...	...	...	...	...	...	...
M 3-8	11.232	10.059	9.687	13.397	11.12	9.631	...	...	...	...	0.67	4.05	5.01	< 14.62	18
M 4-10	13.351	13.105	12.191	15.124	13.236	12.077	...	...	...	...	...	...	...	...	12.1
MaC 1-10	...	...	...	...	...	...	...	...	...	...	5.92	20.62	22.64	< 164.6	...
Mz 2	13.693	13.195	13.034	14.754	13.732	13.056	0.174	...	0.9818	1.219:	0.49	4.75	8.2	11.42	...
NGC 6302	11.255	10.706	9.442	12.557	10.966	9.408	...	...	...	...	32.08	335.9	849.7	537.4	1908
NGC 6578	12.649	9.825	8.934	...	...	...	1.159	1.242:	6.541	10.71	<12.8	16.1	37.31	<355	158.2
Pe 1-6	...	...	...	...	...	...	...	...	...	...	< 4.46	1.53	5.15	< 40.91	...
Pe 2-10	12.14	11.39	10.865	13.91	12.047	10.864	...	...	...	...	...	...	...	...	...
Pe 2-12	11.627	10.947	10.772	12.981	11.682	10.816	...	...	...	...	< 2.21	1.29	6.59	< 186.3	...
Sa 3-104	13.332	12.613	11.809	...	...	...	0.828	1.41	1.23	2.685	1.39	3.45	1.74	< 92.57	...
ShWi 1	13.407	12.831	12.56	14.775	13.428	12.613	...	...	...	...	...	...	...	...	...
Th 3-10	14.404	13.581	12.586	17.645	14.241	12.491	...	...	...	...	< 2.62	3.16	4.81	< 48.22	21.6
Th 3-11	14.395	11.123	10.61	...	...	...	...	...	...	...	...	...	...	...	6.9
Th 3-13	13.674	13.067	11.947	16.138	13.831	11.932	0.556	1.641	2.0	6.828	1.3	8.69	3.15	< 4.17	...
Th 3-19	14.147	13.527	12.87	...	...	...	...	...	...	...	4.51	7.12	< 1.84	< 20.16	...
Th 3-23	14.059	12.821	12.38	16.634	13.863	...	...	...	...	...	...	...	...	...	46.2
Th 3-25	13.866	13.17	12.429	...	...	...	...	...	...	...	...	...	...	...	...
Th 3-26	...	...	...	...	...	...	...	...	...	...	2.43	4.31	< 2.63	< 29.7	10.4
Th 3-33	13.51	12.34	11.9	...	...	...	0.351	0.879	0.491	3.336	0.89	4.76	8.67	< 30.45	...
Th 4-3	13.583	13.223	12.782	14.925	13.702	12.862	...	...	...	...	< 0.785	1.928	< 2.78	< 8.731	...
Th 4-9	14.431	13.529	12.214	16.268	14.617	12.084	0.573	0.892	0.909	1.856	1	1.85	< 1.41	< 15.78	...
Vd 1-5	15.548	15.103	14.569	16.985	15.262	...	...	...	...	...	...	...	...	...	...